Physica D 472 (2025) 134457

Contents lists available at ScienceDirect

Physica D

journal homepage: www.elsevier.com/locate/physd

Almost synchronization phenomena in the two and three coupled Brusselator systems

Ana Mayora-Cebollero [a,b], Jorge A. Jover-Galtier [a,b,*], Fátima Drubi [c], Santiago Ibáñez [c], Álvaro Lozano [b,d], Carmen Mayora-Cebollero [a,b], Roberto Barrio [a,b]

[a] Departamento de Matemática Aplicada, Universidad de Zaragoza, c/Pedro Cerbuna, 12, Zaragoza, 50009, Spain
[b] Instituto Universitario de Matemáticas y Aplicaciones (IUMA), c/Pedro Cerbuna, 12, Zaragoza, 50009, Spain
[c] Departamento de Matemáticas, Universidad de Oviedo, c/Leopoldo Calvo Sotelo, 18, Oviedo, 33007, Spain
[d] Departamento de Matemáticas, Universidad de Zaragoza, c/Pedro Cerbuna, 12, Zaragoza, 50009, Spain

ARTICLE INFO

Communicated by Liang Huang

Keywords:
Coupled systems
Brusselator model
Singular perturbation theory
Bifurcations

ABSTRACT

We present a study of some temporal almost synchronization phenomena of systems of two and three coupled Brusselators: they are approximately synchronized during most of the dynamics, only losing synchronization for small times and quickly returning to an almost synchronized state. Here we show two situations where this phenomenon occurs, one related with codimension-two Hopf–pitchfork bifurcations, and the other one due to the existence of fast–slow dynamics. On the one hand, a detailed characterization of the codimension-two Hopf–pitchfork bifurcations in the model allows us to determine the regions of the parameter space in which this phenomenon occurs. On the other hand, a fast–slow analysis of the two coupled Brusselators, using singular perturbation theory, illustrates the second situation studied here. We next analyze this phenomenon numerically, by explicitly calculating the fraction of time during which different trajectories are almost synchronized. Our results are then extended to the case of three coupled Brusselators.

1. Introduction

A great variety of biological and chemical processes can be studied using models where identical dynamical systems interact with each other through simple coupling mechanisms. Many models of neural networks or diffusively coupled chemical reactors fit this description. Even simple neural models, such as the Hodgkin–Huxley model [1], give rise to complex patterns when neurons are coupled; there are examples ranging from rhythmic patterns occurring in small groups of cells (Central Pattern Generators, CPGs) [2–4] to collective behaviors of large populations of neurons [5,6]. Other interesting examples in biology and chemistry can be found in the analysis of chemical reactors, coupled by allowing substances to move from one reactor to another [7]; such is the case of glycolytic oscillators [8], coupled Brusselator systems [8,9] or even cells [10].

Perhaps the most interesting problems that one can face when working with coupled dynamical systems are related to synchronization phenomena. The scientific community has been fascinated by synchronization for a long time, dating back to 17th century, when Christopher Huygens described the behavior of two pendulum clocks hanging from a wall. We can mention other paradigmatic examples such as the behavior of fireflies, heart pacemaker cells, the neural networks that control circadian rhythms or the synchronization of neurons linked to Parkinson's disease (see Ref. [11] and references therein). All these examples show the relevance of the study of synchronization, not only theoretically but also from the perspective of its application to fields such as Engineering, Chemistry and Medicine.

Many studies on synchronization deal with networks of coupled systems. In this context, a network is said to be *fully synchronized* when its coupled systems oscillate in a coherent way [12–15]. In networks where more than two systems are coupled, *partial synchronization* (also called *clustered synchronization*, *polysynchronization* or *concurrent synchronization*) may also appear [16]. In partial synchronization, the coupled systems split into two or more subgroups, called clusters, in such a way that the oscillators synchronize with one another in the same cluster (i.e. each cluster is fully synchronized), but there is no synchronization among different clusters. Other various weaker forms of synchronization have been proposed in literature, such as practical synchronization [17], phase synchronization [13,18], time-lag synchronization [14], generalized synchronization [19] and collective almost synchronization [20]. The concept of *collective almost synchronization*

* Corresponding author at: Departamento de Matemática Aplicada, Universidad de Zaragoza, c/Pedro Cerbuna, 12, Zaragoza, 50009, Spain.
E-mail addresses: amayora@unizar.es (A. Mayora-Cebollero), jorgejover@unizar.es (J.A. Jover-Galtier), drubifatima@uniovi.es (F. Drubi), mesa@uniovi.es (S. Ibáñez), alozano@unizar.es (Á. Lozano), cmayora@unizar.es (C. Mayora-Cebollero), rbarrio@unizar.es (R. Barrio).

https://doi.org/10.1016/j.physd.2024.134457
Received 18 April 2024; Received in revised form 5 November 2024; Accepted 19 November 2024
Available online 28 November 2024

deals with the distance, measured on the phase space, among orbits of the systems (with or without lag); when all orbits are close enough, i.e. their distances are smaller than a small quantity ε, then the network is said to show collective almost synchronization. However, it is possible to also observe temporal regimes characterized by incomplete synchronization, which in some fields is referred to as partial synchronization in a more general way than in [16]. Existence of intervals of near synchronization are also discussed in [21,22] in the context of mixed-mode oscillations in coupled Fitzhugh–Nagumo oscillators. In this paper, we deal with networks showing collective almost synchronization only in some time intervals. Based on the concepts mentioned above, we provide an appropriate definition for the observed phenomena. Specifically, we connect them with fast–slow dynamics on the model and/or specific bifurcations. It should be noted that our study focuses on models with a small number of coupled systems, in our case two and three chemical Brusselators systems, where we can make a more detailed analysis of the different elements. For larger networks, it may be more appropriate to use the techniques and concepts developed for synchronization in coupled oscillators (Kuramoto models) [14].

Regarding the mathematical study of dynamical systems and their characteristics, it should be noticed that, in a typical natural interaction scenario, the number of involved individual units can be very large, even thousands of elements or more in the case of neural networks. However, the study of models with few elements, even with only two units, can give some insight into the behavior and characteristics of more general or realistic systems. Furthermore, certain coupled systems with only two elements, such as the case of two coupled continuous-flow stirred tank reactors, have a long research history and a great practical and theoretical interest (see [23] and references therein). In particular, synchronization phenomena may occur when only a small number of systems are coupled. Thus, analyzing the coupling of few dynamical systems is both relevant for the characterization of the emerging behaviors, and feasible from an analytical and computational point of view.

In this paper, we study the coupling of Brusselators using a linear diffusion mechanism [9]. The general model for the coupling of two identical dynamical systems can be described as follows. Consider a dynamical system with coordinates $\mathbf{u} \in \mathbb{R}^n$, whose dynamical equation is $\mathbf{u}' = F(\mathbf{u})$, with $\mathbf{u}'$ denoting the time derivative and F an n-dimensional vector field. If two identical copies of this system are considered, with coordinates $\mathbf{u}_1, \mathbf{u}_2 \in \mathbb{R}^n$, the equations describing their coupled evolution are

$$\begin{cases} \mathbf{u}_1' = F(\mathbf{u}_1) + \Lambda(\mathbf{u}_2 - \mathbf{u}_1), \\ \mathbf{u}_2' = F(\mathbf{u}_2) + \Lambda(\mathbf{u}_1 - \mathbf{u}_2), \end{cases} \tag{1}$$

where Λ is an $n \times n$ non-negative definite diagonal matrix. It easily follows that the manifold $\Pi = \{(\mathbf{u}_1, \mathbf{u}_2) \in \mathbb{R}^{2n} : \mathbf{u}_1 = \mathbf{u}_2\}$ is invariant by the flow of (1). The manifold Π is called the synchronization manifold, with each attractor $A \subset \Pi$ determining a synchronized state of the whole system. Bifurcations of A that happen on Π imply a change in the observed synchronization phenomenon. For instance, if A is a hyperbolic attracting equilibrium point that undergoes a super-critical Hopf bifurcation on the invariant manifold Π, it will change into a synchronized periodic state. On the other hand, bifurcations that happen transversely to Π give rise to desynchronization phenomena. Again, if A is a hyperbolic attracting equilibrium point that undergoes a pitchfork bifurcation transverse to Π, it will lose its stability generating two non-synchronized stable stationary states.

Codimension-two bifurcations on a coupled system such as (1) appear when one bifurcation on Π and another one in a direction transverse to Π collide. A simple scenario would be the pitchfork-pitchfork interaction, but it would not unfold particularly rich dynamics. Instead, in this paper we consider codimension-two Hopf–pitchfork (HP in the sequel) bifurcations, which in some cases give rise to very interesting phenomena. HP bifurcations are the results of the interaction between Hopf bifurcations on Π and pitchfork bifurcations in directions transverse to Π. HP bifurcations in a coupled system may arise naturally if the isolated units exhibit a Hopf bifurcation. Codimension-two HP bifurcations lead to planar reductions identical to those of Hopf–Hopf bifurcations, which are studied in Refs. [24,25], and of which there are twelve different cases, classified by Guckenheimer and Holmes (see Table 7.5.2 in Ref. [24]). Some of the essential features of these bifurcations are reviewed for completeness in the Appendix.

The focus of the paper is the study of HP bifurcations and synchronization phenomena of diffusion-coupled Brusselator systems. The Brusselator, as introduced in Ref. [26], is a two-variable system that models an autocatalytic reaction leading to chemical oscillations. The model is based on a set of reactions with input products A, B; final products P, Q; and intermediates X, Y:

$$\begin{aligned} &A \to X, \quad B + X \to Y + P, \\ &2X + Y \to 3X, \quad X \to Q. \end{aligned} \tag{2}$$

Denoting the concentrations of input products by positive constants $A, B > 0$, and with concentrations x and y of the intermediates acting as variables, the equations of the model are

$$\begin{cases} x' = A - (B+1)x + x^2 y, \\ y' = Bx - x^2 y. \end{cases} \tag{3}$$

First quadrant of the (x, y) plane is forward invariant by the flow, and the system exhibits a supercritical Hopf bifurcation when $B = A^2 + 1$. If $B < A^2 + 1$, there is a unique globally attracting equilibrium point at $(A, B/A)$, while for $B > A^2 + 1$ there is a unique globally attracting periodic orbit.

Consider now two identical Brusselators, identified by their coordinates (x_1, y_1) and (x_2, y_2). The resulting coupled Brusselator system (2-CBS in the sequel) evolves according to (1), with F in this case describing the dynamics (3) of a single Brusselator:

$$\begin{cases} x_1' = A - (B+1)x_1 + x_1^2 y_1 + \lambda_1(x_2 - x_1), \\ y_1' = Bx_1 - x_1^2 y_1 + \lambda_2(y_2 - y_1), \\ x_2' = A - (B+1)x_2 + x_2^2 y_2 + \lambda_1(x_1 - x_2), \\ y_2' = Bx_2 - x_2^2 y_2 + \lambda_2(y_1 - y_2), \end{cases} \tag{4}$$

with coupling parameters $\lambda_1, \lambda_2 \geq 0$. The first octant with positive values of all the variables is forward invariant under the flow, and so is the synchronization manifold Π.

Numerical solutions show differences in the timescales of the system, which motivates to use the tools of singular perturbation theory to characterize the dynamics. Singular perturbation theory deals with the description of systems with two differentiated timescales, allowing for an explicit separation of fast and slow evolution [27–29]. This characterization of dynamics has been proven to be very useful for the analysis of many dynamical systems, such as cardiac cell models [30–32], neural models [6,33] and others [34].

The 2-CBS has been studied from different perspectives. In Refs. [35–37], numerical evidences of the existence of strange attractors were given. With this motivation, in Ref. [38] (see also Ref. [39]), an analytical proof of its existence is provided. Recently (see Ref. [9]), a detailed numerical exploration of the chaotic dynamics displayed by the family of coupled Brusselators has been carried out. On the other hand, Ref. [40] presents a study of HP singularities that are unfolded in the 2-CBS. A rich variety of cases are reported, including bifurcations of codimensions two, three and four, and those that may unfold chaotic dynamics are discussed. In total, at least eight of the twelve cases described in the classification by Guckenheimer and Holmes were found.

In this paper, we analyze one of the codimension-two cases of HP bifurcation that is unfolded by the 2-CBS. It is a case that allows explaining the appearance of "temporal almost synchronization". If the synchronization manifold Π of a coupled system becomes unstable through a bifurcation, stable limit cycles may appear outside of

Π. Temporal almost synchronization occurs when these limit cycles, representing unsynchronized states of the system, stay close to Π for long parts of their periods. In other words, coupled systems are said to go through temporal almost synchronization when for the most part of their time evolution they stay approximately synchronized, while only for small times they are clearly out of synchronization. This interesting phenomenon can be studied in the 2-CBS system by both a numerical analysis and a study of bifurcations leading to these phenomena.

This paper is organized as follows. Section 2 shows a detailed description of HP bifurcations in the 2-CBS model and the changes in the limit cycles of the system. Section 3 describes how some of these cases exhibit temporal almost synchronization. Moreover, a mathematical study of the phenomenon is given. Section 4 considers the concept of almost synchronization to a fast–slow regime of the 2-CBS model. In particular, singular perturbation theory is applied to both a single Brusselator and two coupled Brusselators, showing how temporal almost synchronization emerges from this analysis. Section 5 extends the analysis of previous sections to the study of three coupled Brusselators, characterizing their dynamical properties. Finally, conclusions are presented in Section 6. The theory of codimension-two Hopf–pitchfork bifurcations is reviewed in the Appendix.

2. Bifurcations in the 2-CBS model

Bifurcations in the 2-CBS model are responsible for the loss of stability of the synchronization manifold. Elementary bifurcations that occur in the 2-CBS model (4) have been studied in Refs. [9,38,40]. In this section, we focus on the characterization of Hopf–pitchfork (HP) bifurcations, following the classical theory of bifurcations [24]. A brief review of the theory is presented in the Appendix.

For all parameter values there is an equilibrium point at $(A, B/A, A, B/A)$ that belongs to the synchronization manifold $\Pi = \{x_1 = x_2, y_1 = y_2\}$. Recall that the dynamics on Π is that of the isolated Brusselator. Moreover, the 2-CBS is invariant under the symmetry

$$(x_1, y_1, x_2, y_2) \to (x_2, y_2, x_1, y_1). \tag{5}$$

In Ref. [9] it is proven that the system may exhibit up to five equilibrium points. Under generic conditions, there is a pitchfork bifurcation at $(x_1, y_1, x_2, y_2) = (A, B/A, A, B/A)$ for all parameter values in the hypersurface

$$M_P = \left\{ (A, B, \lambda_1, \lambda_2) \in V : B = \frac{(A^2 + 2\lambda_2)(1 + 2\lambda_1)}{2\lambda_2} \right\}, \tag{6}$$

where $V = \{(A, B, \lambda_1, \lambda_2) \in \mathbb{R}^4 : \ A > 0, B > 0, \lambda_1 > 0, \lambda_2 > 0\}$. This bifurcation is transverse to the synchronization manifold.

The Jacobian matrix has at least one pair of pure imaginary eigenvalues on the bifurcation hypersurfaces of codimension 1,

$$M_H^1 = \Big\{ (A, B, \lambda_1, \lambda_2) \in V : B = 1 + A^2 + 2(\lambda_1 + \lambda_2), \\ \lambda_1 > \frac{4\lambda_2^2 + 2\lambda_2 A^2 - A^2}{2A^2} \Big\}, \tag{7}$$

which corresponds to the Hopf bifurcations occurring transversely to Π, and

$$M_H^2 = \big\{ (A, B, \lambda_1, \lambda_2) \in V : B = 1 + A^2, \\ A^2(1 + 2\lambda_1 - 2\lambda_2) + 4\lambda_1\lambda_2 \neq 0 \big\}, \tag{8}$$

which corresponds to Hopf bifurcation for the isolated Brusselator system on the invariant plane Π.

The hypersurfaces M_P and M_H^2 have a common border along the bifurcation surface

$$M_{HP} = \Big\{ (A, B, \lambda_1, \lambda_2) \in V : B = 1 + A^2, \\ \lambda_1 = \frac{(-1 + 2\lambda_2)A^2}{2(A^2 + 2\lambda_2)}, \ \lambda_2 > \frac{1}{2} \Big\}, \tag{9}$$

on which the Jacobian matrix at $(x_1, y_1, x_2, y_2) = (A, B/A, A, B/A)$ has a pair of pure imaginary eigenvalues and a zero eigenvalue. Therefore, M_{HP} is a bifurcation surface of Hopf–pitchfork singularities of codimension at least 2. In Ref. [40], it is proved that several cases of codimension 2, 3 and 4 are generically unfolded by the 2-CBS.

On the other hand, if the appropriate generic conditions are satisfied, the 2-CBS exhibits a saddle–node bifurcation at an equilibrium point outside the synchronization manifold for parameter values on the hypersurface

$$M_{SN} = \Big\{ (A, B, \lambda_1, \lambda_2) \in V : \lambda_2 = \frac{4A^2(1 + 2\lambda_1)^2}{(1 + B + 2\lambda_1)^2}, \\ B > 3 + 6\lambda_1 \Big\}. \tag{10}$$

So, hypersurface M_{SN} separates two regions with either 1 or 5 equilibrium points. Transition from 5 to 3 (or from 1 to 3) will take place when parameters cross the hypersurface M_P corresponding to the pitchfork bifurcation.

Results in Ref. [40] show that the 2-CBS exhibits at least eight of the twelve cases of codimension-two HP bifurcations. In Figure 4 of Ref. [40] one can see a partial map of the different cases that are detected for parameter values $(A, \lambda_2) \in [0, 10] \times [0, 10]$. For instance, when $A = 4 = A^*$ and $\lambda_2 = 2 = \lambda_2^*$, there is an HP bifurcation of type VIa for which the emerging invariant torus is attracting. Note that parameters B and λ_1 at the bifurcation point are given by the formulas that characterize the M_{HP} surface (9), namely $B = 17 = B^*$ and $\lambda_1 = 6/5 = \lambda_1^*$. All numerical explorations in this paper are done for parameter values close to $(A^*, B^*, \lambda_1^*, \lambda_2^*)$.

Fig. 1 shows the results of the exploration along a straight line in the parameter space with $A = A^*$, $\lambda_1 = \lambda_1^* + 0.01$, $\lambda_2 = \lambda_2^*$ and $B \in [16.98, 17.12]$, a small interval containing B^*. Panels (a) and (b) correspond to local bifurcations of limit cycles and panel (c) to bifurcations of equilibrium points (these bifurcation diagrams were obtained with the MATCONT continuation software [41,42]). In panel (d), the spike-counting (SC) technique [43] is used to explore the parametric plane (B, λ_1). This technique detects the number of maximum points during a period (of variable x_1) of an orbit and assigns a color to each value (when an orbit reaches the maximum possible number of assigned maxima, we assume that it shows either chaotic behavior or periodic behavior with a large number of maxima). Six different orbits (green) are provided in the upper part of Fig. 1 to illustrate the changes in the phase-space when the different bifurcations are crossed. It should be noted that the numbering of each of the six cases agrees with that used in the theoretical bifurcation diagram displayed in Fig. A.16 in the Appendix. The synchronization manifold is shown in light blue color.

The transition from Case 1 to Case 2 of Fig. 1 illustrates the Hopf bifurcation (H) that occurs in the synchronization manifold Π: the attracting equilibrium point on Π changes into a saddle node and an attracting periodic orbit emerges (compare with bifurcation P_1^- in Fig. A.16). The bifurcation point is clearly visible in panels (b) and (c). In the transition from Case 2 to Case 3, a branch point of periodic orbits is crossed. As a result, the periodic orbit on Π loses its stability and a pair of attracting periodic orbits appears outside the synchronization manifold (compare with bifurcation P_3 in Fig. A.16). This bifurcation is also shown in panels (a) and (b). A Neimark–Sacker bifurcation (NS) occurs in the transition from Case 3 to Case 4 (bifurcation H in Fig. A.16) and an attracting invariant torus emerges. Note that the torus is only present in a very small range of parameters. In panel (a), one can check how the stable periodic orbit exhibited in Case 3 loses its stability. In Case 5, the attracting torus has disappeared and the orbit goes to an equilibrium point outside the synchronization manifold. Upper panel in Fig. 1 does not show any change in the transition from Case 5 to Case 6, but there is indeed a bifurcation; namely, there is a pair of repelling periodic orbits that disappears through a Hopf bifurcation at an equilibrium point outside the synchronization manifold (this corresponds to bifurcation P_4 in Fig. A.16). This bifurcation is clear in panels (a) and (c).

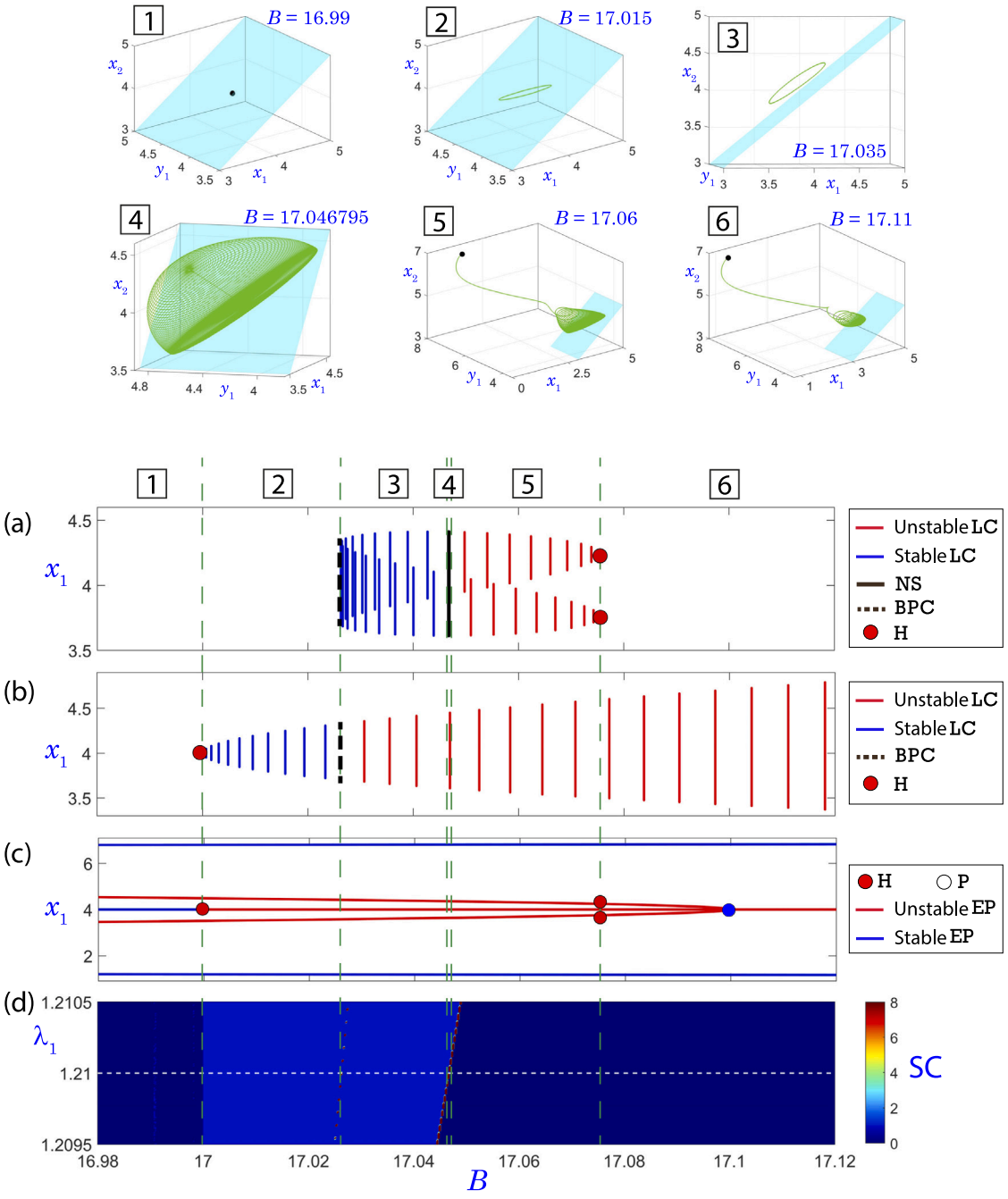

Fig. 1. The bifurcation diagrams of limit cycles (LC) outside the synchronization plane Π and in Π are represented in panels (a) and (b), respectively (NS: Neimark–Sacker bifurcation, H: Hopf bifurcation, BPC: Branch point cycle bifurcation). In panel (c), the bifurcation diagram of equilibrium points (EP) is shown (H: Hopf bifurcation, P: Pitchfork bifurcation). In panel (d), the spike-counting sweeping in the parametric plane (B, λ_1) is drawn. At the top, some orbits for different values of B are represented in green and the synchronization plane is shown in light blue. The initial conditions used to integrate these orbits are $(x_1, y_1, x_2, y_2) = (A - \delta, B/A - \delta, A + \delta, B/A + \delta)$ where $\delta = 0.01$. In the representations, $A = 4.0$, $\lambda_2 = 2.0$ and $\lambda_1 = 1.21$ (this value of λ_1 is marked in panel (d) with a horizontal white dashed line).

Regions corresponding to parameter values where orbits tend to an equilibrium (0 spikes) appear in the darkest blue color in panel (d). A lighter blue color marks the region where the system exhibits an attracting periodic orbit (1 spike). Panel (d) also shows a very thin region in brown color, corresponding to parameter values for which the phase portrait contains an attracting torus, such as the one shown in Case 4; in these situations, the number of spikes explodes.

Fig. 2 shows a wider region in the parameter space surrounding the HP bifurcation point. Panel (a) shows the equilibrium point analysis and the bifurcation diagram described above, while panel (b) shows the spike-counting sweeping of the area; the transition from 0 to 1 spikes can be seen. Bifurcation curves in both diagrams were obtained with MATCONT [41,42]. In both panels, the vertical black dashed line represents a Hopf bifurcation on the synchronization manifold, which corresponds to the transition from Case 1 to Case 2 in Fig. 1. There is a branch point of limit cycles (BPC) along the blue line that emerges from the HP bifurcation point (green), which corresponds to the transition from Case 2 to Case 3 in Fig. 1. Tori emerge when parameters cross the NS bifurcation curve (green), which corresponds to the transition from Case 3 to Case 4 in Fig. 1. A Hopf bifurcation occurs outside the synchronization plane along all solid black bifurcation curves, included the one that emanates from the HP bifurcation point, which corresponds to the transition from Case 5 to Case 6 in Fig. 1. The red

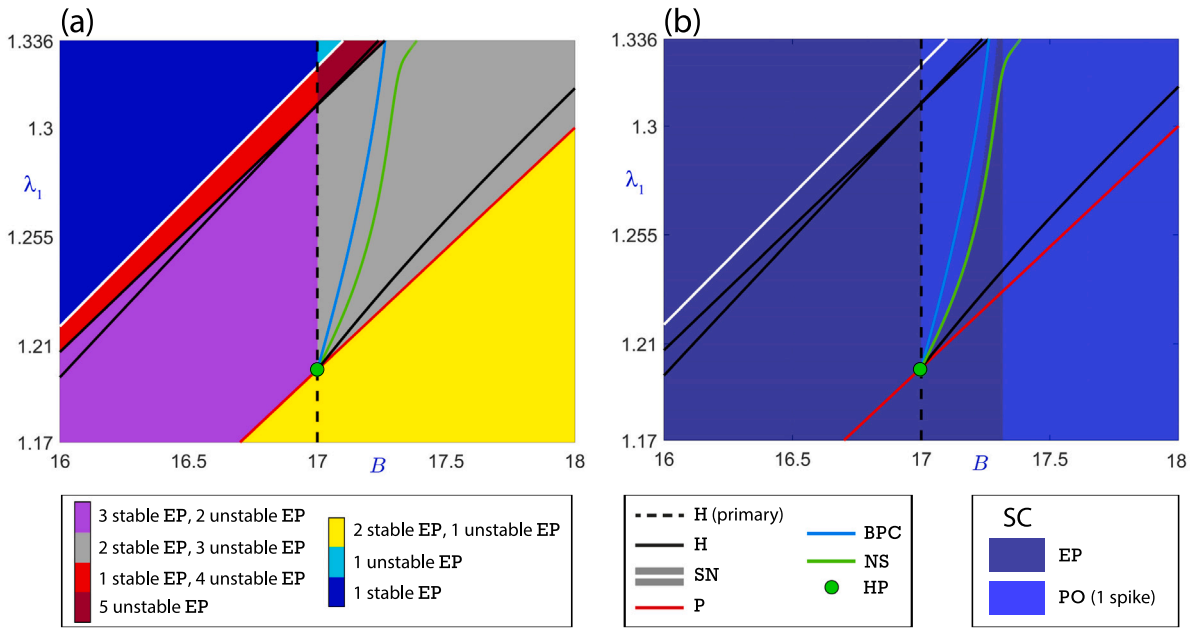

Fig. 2. In panel (a), number of equilibrium points and their stability in a region of the biparametric plane (B, λ_1). In panel (b), spike-counting sweeping of that parametric plane. In both panels some bifurcations are marked. The values of the fixed parameters are $A = 4.0$ and $\lambda_2 = 2.0$.

line corresponds to a pitchfork bifurcation (P) at the equilibrium point on the synchronization plane. Note that for parameter values below the pitchfork bifurcation line (yellow region in panel (a)) the system exhibits three equilibrium points, while above it there are five equilibrium points. There is also a saddle–node bifurcation (SN) of equilibria along the white line; there, the 2-CBS changes from exhibiting five to only one equilibria. One should compare the bifurcation diagram in panel (a) of Fig. 2 with that in Fig. A.16 and notice that colors of all bifurcation curves are in correspondence, except for the case of the curve HC (Heteroclinic cycle) in Fig. A.16, which does not appear in the bifurcation diagram shown in panel (a). Correspondence between bifurcation curves in the full system and those in a 2-dimensional truncated normal form (see (A.5)) is explained in the Appendix.

Indeed, as already mentioned, when general unfoldings of an HP bifurcation are considered, it is not possible to identify a bifurcation corresponding to the heteroclinic cycle configuration exhibited in truncated normal forms. However, the ghost of such a bifurcation is present, since the invariant tori disappear in an abrupt way from the phase space. The torus shown to illustrate Case 4 in the upper panel of Fig. 1 is very close to forming an heteroclinic cycle configuration (that is, it is close to the theoretical HC curve shown in Fig. A.16).

For parameter values corresponding to Case 4 in Fig. 1 the 2-CBS exhibits five equilibrium points: a point, that we denote as P_0, contained in the synchronization plane and two pairs of symmetric equilibria, $P_\pm$ and $Q_\pm$, outside the synchronization plane. We assume that the points $P_\pm$ are those involved in the HP bifurcation. Local analysis (see Section 3 in Ref. [40]) shows that the Hopf–pitchfork singularity exhibits an attracting three-dimensional center manifold. Bifurcations occur in this center manifold. Fig. 3 shows again the invariant torus already displayed in Fig. 1 (orbit 4) in the (x_1, y_1, x_2) phase space and, additionally, a schematic information (panel (a)) about the ghost of the heteroclinic cycle configuration shown in panel (b). The elements of the cycle are the equilibrium points P_0 and P_+, the periodic orbit PO_{II} contained in the synchronization plane, and their stable (W^s) and unstable (W^u) invariant manifolds. We use the notation $P_\pm(m, n)$ and $Q_\pm(m, n)$ to indicate that an equilibrium point has stability (resp. unstability) index m (resp. n) in the four-dimensional system. In panel (b), $W^u(P_0) \setminus \{P_0\}$ is contained in the invariant manifold $W^s(PO_{II})$. And also, the invariant manifolds $W^u(PO_{II})$ and $W^s(P_+)$ are close each other and there is an almost coincidence of branches of the one-dimensional invariant manifolds $W^u(P_+)$ and $W^s(P_0)$. This almost coincidence gives rise to the almost heteroclinic cycle. This scenario allows us to understand how there is a chance for chaotic dynamics. Shilnikov homoclinic orbits to P_+ and codimension-two heteroclinic cycles involving P_0, P_+ and PO_{II} are likely to appear. Nevertheless, our numerical results reveal that although possible, chaotic behavior emerging from HP bifurcations has no relevance in the model, at least in the parameter region that we are exploring.

The existence of the shadow of a heteroclinic cycle has, however, other dynamical consequences of remarkable relevance. In their approximation to that ghost, invariant tori approximate a part of the synchronization manifold, namely, the unstable manifold of the equilibrium point P_0. As a consequence, as an orbit approaches the torus it will exhibit large temporal almost synchronization. This phenomenon is certainly more general: any orbit converging to an attractor that is totally or partially close to the synchronization manifold will present transits of variable length during which it will be very close to be synchronized.

3. Almost synchronization

As already mentioned, when a trajectory is close to the synchronization plane, variables x_1 and y_1 will be close, respectively, to variables x_2 and y_2. In order to quantify this closeness, we introduce the notion of β_ε *almost synchronization*.

Definition 1. Let $(x_1(t), y_1(t), x_2(t), y_2(t))$ be a solution of the 2-CBS defined in an interval $[0, T]$. Fix $\epsilon_0 > 0$ and take ϵ such that $0 < \varepsilon \le \epsilon_0$, let us consider the following fraction:

$$\beta_\varepsilon = \frac{m(I_\varepsilon)}{T}, \tag{11}$$

where T is assumed to be large enough, m denotes the Lebesgue measure on the real line and

$$I_\varepsilon = \{t \in [0, T] \ : \ \max\{|x_1(t) - x_2(t)|, |y_1(t) - y_2(t)|\} \le \varepsilon\}. \tag{12}$$

We say that the solution is β_ε *almost synchronized* if $\beta_\varepsilon > 0$, i.e. if, for some fraction β_ε of the total time T, the distances between x_1 and x_2 and between y_1 and y_2 are below the threshold ε. In particular, a fully synchronized solution is β_ε almost synchronized with $\beta_\varepsilon = 1$

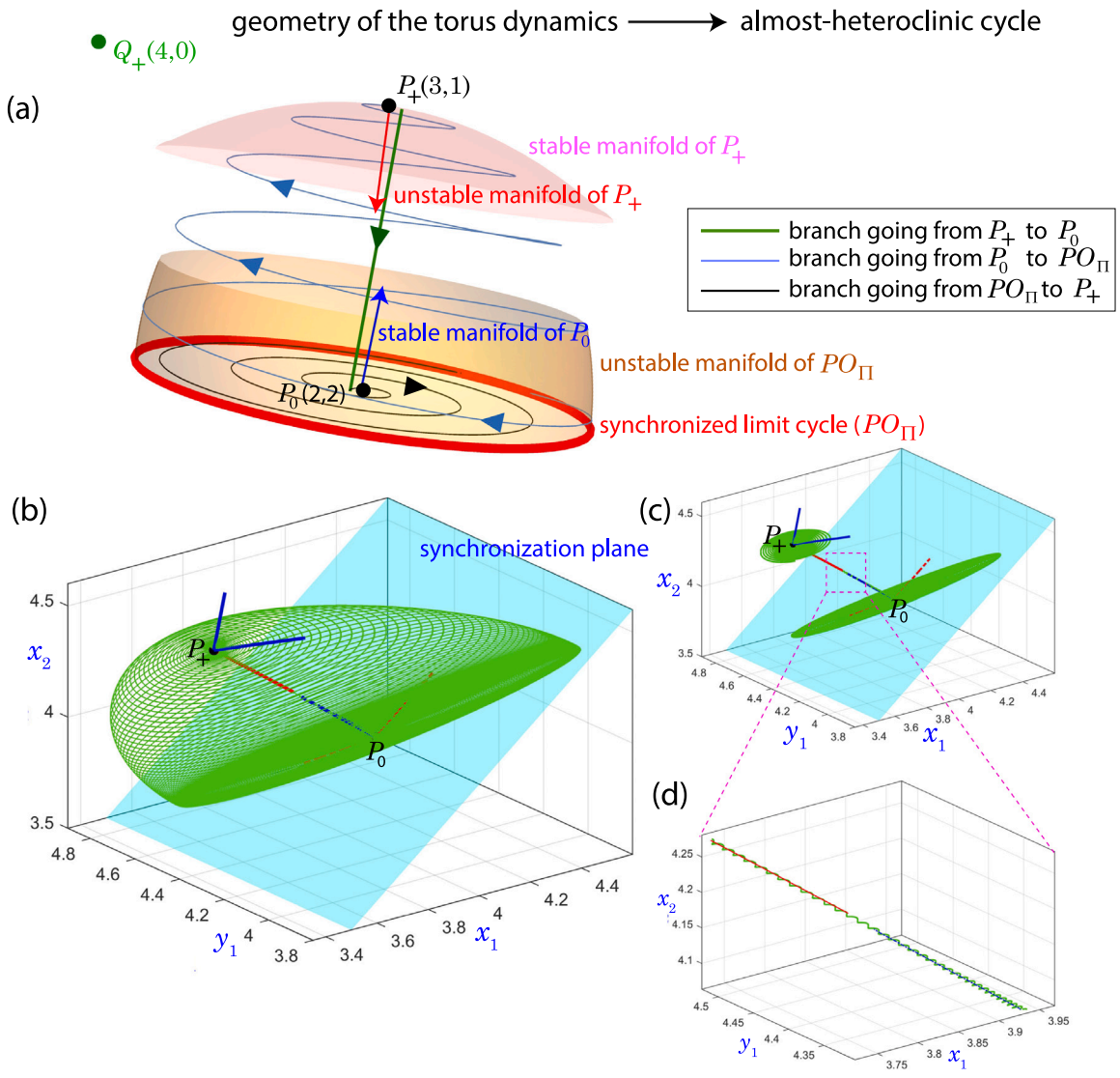

Fig. 3. In panel (a), a 3D theoretical scheme of the stable and unstable manifolds of the unstable limit cycle PO_Π, and the unstable equilibria P_0 and P_+ is shown, together with a sketch of an orbit showing temporal almost synchronization. In panel (b), this orbit is shown in green in the (x_1, y_1, x_2) phase space, together with either the eigenvectors, if real, or their real and imaginary parts, if complex, of the equilibrium points P_0 and P_+, shown in blue if stable and in red if unstable. The orbit stays close to the synchronization plane when it evolves from P_0 towards the limit cycle PO_Π, hence β_ϵ, defined by (11), is non-zero for appropriate values of ϵ. Panel (c) shows only part of the orbit, in order to better present its inside part: when the orbit completes the dome-like structure starting from PO_Π and following the stable manifold of P_+, it jumps towards P_0 along the directions of the unstable manifold of P_+ and the stable manifold of P_0. This part of the orbit is further enlarged in panel (d). The initial conditions used to integrate this orbit are $(x_1, y_1, x_2, y_2) = (A-\delta, B/A-\delta, A+\delta, B/A+\delta)$, where $\delta = 0.01$ and with parameters $A = 4.0$, $B = 17.046795$, $\lambda_1 = 1.21$ and $\lambda_2 = 2.0$.

for any ϵ. Moreover, a solution is said *temporally* (resp. *fully*) *almost synchronized* when there exists $\epsilon \in (0, \epsilon_0]$ such that the solution is β_ϵ almost synchronized with $0 < \beta_\epsilon < 1$ (resp. $\beta_\epsilon = 1$).

Remark 1. Note that ϵ_0 is a maximum threshold introduced to establish what can be considered almost synchronization. Otherwise, without a threshold, any solution could be said β_ϵ almost synchronized only by taking ϵ large enough. Along the paper we consider $\epsilon_0 = 0.1$.

In the 2-CBS, almost synchronization is observed when parameters cross the branch point of limit cycles (see the transition from Case 2 to Case 3 in Fig. 1 and also the blue bifurcation curve in panel (b) of Fig. 2). Through that bifurcation, the limit cycle on the synchronization manifold loses its stability and an attracting limit cycle emerges from the synchronization manifold Π (Case 3). Beyond the bifurcation point, the limit cycle moves away from Π, hence full almost synchronization can be briefly detected as long as the distance between the limit cycle and Π is not greater than ϵ_0. Far from the bifurcation point no almost synchronization occurs, as the limit cycle lays far from Π. However, after suffering an NS bifurcation, an attracting invariant torus appears (Case 4), part of which lays close to Π; in this situation, temporal almost synchronizations appear.

Continuing the periodic orbits that emerge through a branch point of limit cycles and fixing a collection of thresholds, one can compute the fraction β_ϵ for each case. Fig. 4 shows the results of such exploration along the bifurcation line already considered in Fig. 1. Principal bifurcation events outside Π in this context are drawn in panel (a): the branch point of limit cycles and the NS bifurcation. As we can observe in panel (b), for values of B below the branch point of limit cycles, $\beta_\epsilon = 1$ for all thresholds ϵ because there is an attracting limit cycle contained in the synchronization manifold (gray color corresponds to β_ϵ almost synchronization for all selected thresholds). Once the parameter B crosses the branch point of limit cycles, the periodic solution briefly exhibits β_ϵ almost synchronization for different values of ϵ; the fraction β_ϵ decreases rapidly as the distance between the limit cycle and the

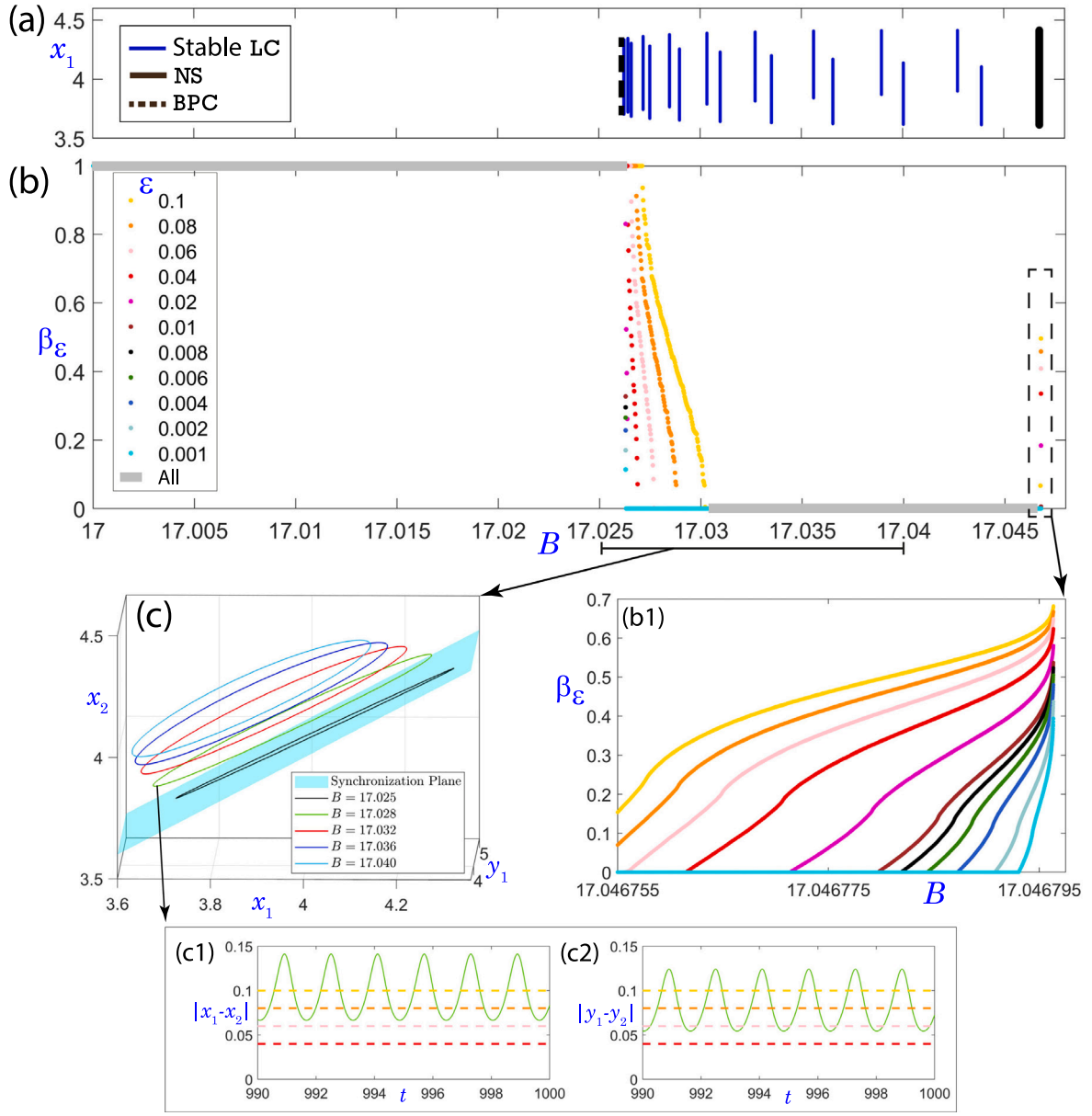

Fig. 4. In panel (a), the bifurcation diagram of limit cycles of the periodic orbit outside the synchronization plane Π is shown (similar to panel (a) in Fig. 1). In panel (b), the β_ε almost synchronization is studied for different values of the threshold ε and of the parameter B. In panel (b1), a zoom of the last zone of panel (b) is presented to see what really happens. In panel (c), the synchronization plane Π, the stable orbit on such plane for $B = 17.025$ and the stable orbits outside the plane Π for different values of B are drawn. In panels (c1) and (c2), the differences $|x_1 - x_2|$ and $|y_1 - y_2|$ of the green orbit ($B = 17.028$) of panel (c) are shown, respectively. In both graphics, the dashed lines represent some thresholds with the same code color as the one in the legend of panel (b). The initial conditions used to obtain these figures are $(x_1, y_1, x_2, y_2) = (A - \delta, B/A - \delta, A + \delta, B/A + \delta)$ where $\delta = 0.01$ and the values of the parameters are $A = 4.0$, $\lambda_1 = 1.21$ and $\lambda_2 = 2.0$.

synchronization plane increases (panel (c)). It is noticeable that this decrease is not instantaneous, but slightly progressive, which indicates that some parts of the orbit lay closer to Π than others (panels (c1) and (c2) for $B = 17.028$ and different values of ε following colors in legend of panel (b)). Eventually, the limit cycle lays far enough from Π so, for large enough values of B after the branch point, $\beta_\varepsilon = 0$ for all selected ε.

Panel (b) in Fig. 4 also shows that the β_ε almost synchronization is linked to the invariant torus analyzed in Fig. 3. It is again clear that this phenomenon occurs in a very small range of parameters, and β_ε almost synchronization is achieved for all considered threshold ε very rapidly after the NS bifurcation. This fast evolution from a limit cycle to a much larger invariant torus could be related to the existence of torus canards in the system (see Ref. [44]).

This area of interest has been enlarged in panel (b1). As the torus increases in size and approaches the ghost of the heteroclinic cycle configuration and therefore also close to the synchronization manifold, more thresholds are reached. For parameter values close to $B = 17.046795$ all selected thresholds have been reached. The corresponding β_ε values appear to converge to some $\beta^* < 1$. This value provides the fraction of time that a solution on the torus is close to the synchronization manifold (with respect to a given threshold); most of the rest of the time the system stays close to the equilibrium point outside the synchronization manifold (either P_+, as in Fig. 3, or P_-).

In Fig. 5, solutions of the 2-CBS that correspond to orbits close to an attracting torus are shown for different values of B. For each parameter value, graphs for all variables are plotted together with two graphs (red color) corresponding to the differences $|x_1(t) - x_2(t)|$ and $|y_1(t) - y_2(t)|$.

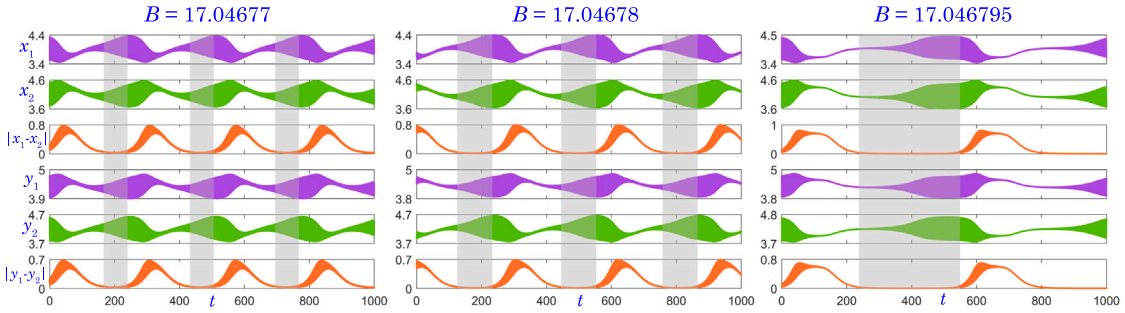

Fig. 5. Representation of the time series of the four variables of 2-CBS and the differences $|x_1 - x_2|$ and $|y_1 - y_2|$ for three different values of parameter B in the rightmost region analyzed in panels Fig. 4.b and 4.b1. The gray shaded stripes in the three subplots highlight regions of the orbit that are close to the synchronization plane, and where almost synchronization occurs. The initial conditions used for the representations are $(x_1, y_1, x_2, y_2) = (A - \delta, B/A - \delta, A + \delta, B/A + \delta)$ where $\delta = 0.01$ and the corresponding values of the parameters are $A = 4.0$, $\lambda_1 = 1.21$ and $\lambda_2 = 2.0$.

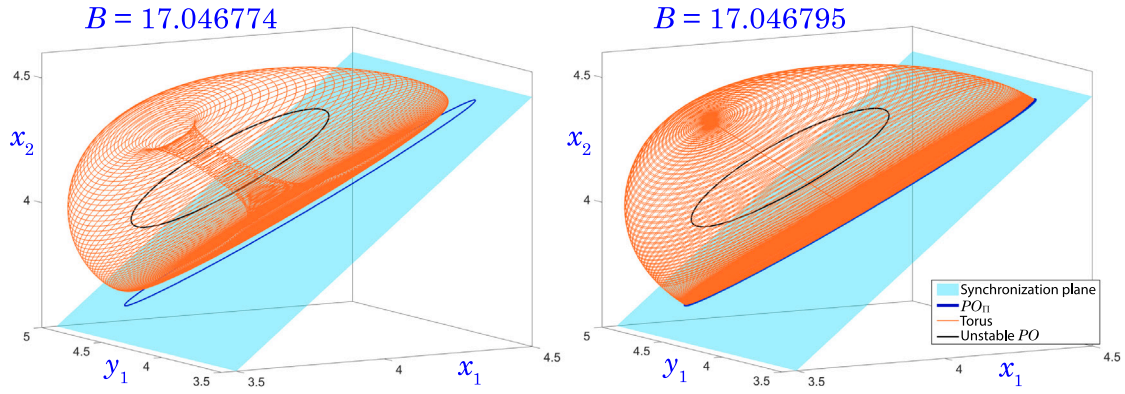

Fig. 6. Representation of a torus-shaped orbit (an example of β_ϵ almost synchronization) and two unstable periodic orbits (one of them on the synchronization plane Π) for two different values of the parameter B. The initial conditions used for both representations are $(x_1, y_1, x_2, y_2) = (A - \delta, B/A - \delta, A + \delta, B/A + \delta)$ where $\delta = 0.01$ and the corresponding values of the parameters are $A = 4.0$, $\lambda_1 = 1.21$ and $\lambda_2 = 2.0$.

Vertical gray stripes are used to mark intervals of time where almost synchronization occurs. As the invariant torus approaches the ghost of a heteroclinic cycle configuration the width of the stripes increases, indicating larger almost synchronization time. Orbits approaching invariant tori are depicted in Figs. 6 and 7 (multimedia available online) for two different values of B, together with a plot of the synchronization plane to illustrate how the distance between such invariant manifold and the tori decreases as B increases. The plot of the right shows an orbit exhibiting an almost heteroclinic cycle.

4. Almost-synchronization in a fast–slow regime of the coupled Brusselator system

Almost synchronization is not limited to situations such as those presented in Section 3, but it can occur in many different regimes of parameters. In this section, we show how almost synchronization can also be explained by a fast–slow analysis of the system and the emergence of critical manifolds with several attracting regions which distribute the trajectories near and far from the synchronization plane.

The Brusselator system (3) shows, for certain values of its parameters, great changes in the speed of the evolution along its stable orbit. Typically, systems showing two different timescales can be written as

$$\mathbf{u}' = F(\mathbf{u}, \tau), \tag{13}$$

with $\mathbf{u} \in \mathbb{R}^n$ the coordinates of the system, F a family of vector fields on $\mathbb{R}^n$, and $0 < \tau \ll 1$ the small parameter determining the difference in time scales. This difference can be made explicit by taking the limit $\tau \to 0$, which is the starting point of singular perturbation theory [45]. In many cases, variables can be characterized as fast and slow, allowing for a clear separation of both types in the system of differential equations [27,28]. However, this is not necessary, as the form presented in (13) is general and allows for a full fast–slow analysis of the dynamics [29]. This will be the approach followed in the paper.

The $\tau \to 0$ limit describes the situation in which slow dynamics of system (13) is neglected, and the resulting set of equations, called the layer system, describes only the fast dynamics of the original system. Equilibrium points of the layer system conform the critical manifold of the system, $S = \{\mathbf{u} \in \mathbb{R}^n : F(\mathbf{u}, 0) = 0\}$. Fenichel's theorem [45] proves the existence of invariant slow manifolds close to normally hyperbolic regions of the critical manifold. When normal hyperbolicity is lost, the system may enter new fast phases of dynamics, potentially allowing for the existence of limit cycles with combined fast and slow evolution. In some cases, movement through fold points causes the system to stay close to repelling regions of S for long times, leading to the appearance of interesting trajectories called canards, that have a great relevance in the description of dynamics [46,47].

The Brusselator system can be described using the singular perturbation theory, which gives some insight on its dynamical properties. Here we present this analysis, as well as its extension to the 2-CBS and a brief analysis of almost synchronizations in this regime.

4.1. Fast–slow analysis of a single Brusselator

In the following, we will assume that the rates of reactions (2) are not equal [48]: the rates of the first and the last equations will be τ, while the rates of the other two equations will be kept equal to 1. The modified equations of the Brusselator model are therefore

$$\begin{cases} x' = \tau(A - x) - Bx + x^2 y, \\ y' = Bx - x^2 y. \end{cases} \tag{14}$$

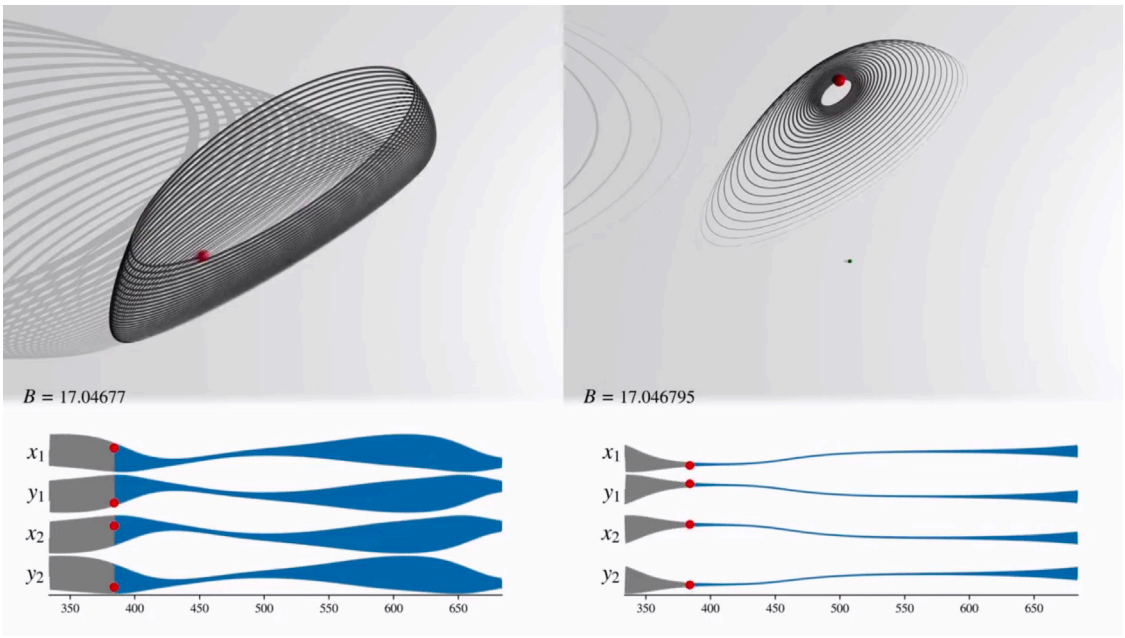

Fig. 7. Static figure taken from the multimedia file illustrating dynamically Figs. 5 and 6: Evolution of the torus-shaped orbits for $B = 17.046774$ (left) and $B = 17.046795$ (right), with the same initial conditions as in Fig. 6, showing the projections of the orbits onto the (x_1, x_2, y_1) space (top) and the evolution of all four variables with respect to time (bottom). Multimedia available online.

The modified system has the same equilibrium point, $(A, B/A)$, which now is stable if $B < \tau + A^2$ and unstable if $B > \tau + A^2$. In the following it will be assumed that the equilibrium point is unstable, in order to characterize the stable limit cycle.

In the range of values $0 < \tau \ll 1$, the system exhibits two different time scales, fast and slow. The fast and slow time scales can be completely separated by considering the limit $\tau \to 0$; by taking this limit in (14), the layer system is obtained:

$$\begin{cases} x' = -Bx + x^2 y, \\ y' = Bx - x^2 y. \end{cases} \tag{15}$$

Equilibrium points of the layer system conform the critical manifold of system (14) $S = S_1 \cup S_2$, with

$$S_1 = \{(0, y) : y \geq 0\}, \quad S_2 = \left\{ \left(x, \frac{B}{x} \right) : x > 0 \right\}. \tag{16}$$

This is a one-dimensional manifold in state space, so (14) is actually a slow–fast system. However, since both variables exhibit fast and slow dynamics, it is not in standard form. A detailed analysis of singular perturbation theory for non-standard form systems can be found in [29].

The critical manifold is normally hyperbolic everywhere except at a single fold point $(\sqrt{B}, \sqrt{B}) \in S_2$. This divides the S_2 into attracting S_2^a and repelling S_2^r regions:

$$\begin{aligned} S_2^a &= \left\{ \left(x, \frac{B}{x} \right) : x > \sqrt{B} \right\}, \\ S_2^r &= \left\{ \left(x, \frac{B}{x} \right) : 0 < x < \sqrt{B} \right\}, \end{aligned} \tag{17}$$

while the S_1 branch is always attractive. The critical manifold and its components are plotted in Fig. 8(a), together with the equilibrium point; assuming it is unstable implies that $A < \sqrt{B}$, hence it is located on S_2^r.

The next step in the study of the fast–slow dynamics of the system is the computation of the layer system, which describes the slow evolution of the system. Notice, however, that a qualitative description of slow dynamics along the critical manifold shown in Fig. 8(a) does not account for the appearance of limit cycles: for a system starting in S_2^r, it may evolve towards the fold point and then jump onto the attracting S_1 branch; but, as this branch lacks a fold point, the system would never return to S_2^r. A similar situation was described in [49] in the general framework of autocatalator models. As in our case, the presence of cubic terms in the dynamical equations causes the fast–slow analysis to require at least $O(\tau)$ terms in order to fully characterize limit cycles.

In this case, we analyze the layer system by computing the slow manifold as a perturbation of the critical manifold (16) [29]. According to Fenichel's theorem [45], for $\tau > 0$ there exist invariant slow manifolds close to the critical manifold S, outside a neighborhood of the fold point. These slow manifolds can be assumed to be locally a graph: thus, for the $S_{1,\tau}$ slow manifold close to the S_1 branch, let us consider x as a function of y:

$$x \equiv x_{1,\tau}(y) = \tau \phi(y) + O(\tau^2). \tag{18}$$

with $\lim_{\tau \to 0} x_{1,\tau}(y)$ being S_1. As the slow manifold is invariant, on it we have $x' = \frac{dx_{1,\tau}}{dy} y'$; substituting (14) yields $\phi(y) = \frac{A}{B}$.

Slow dynamics of the system can be described by rescaling the time by τ, introducing new derivatives $\dot{x} = x'/\tau$, $\dot{y} = y'/\tau$. Thus, (14) when restricted to $S_{1,\tau}$ and considering the limit $\tau \to 0$ yields the following layer system:

$$\begin{cases} \dot{x} = 0, \\ \dot{y} = A. \end{cases} \tag{19}$$

The x variable is constant, while y increases slowly along the slow manifold $S_{1,\tau}$.

On the other hand, outside a neighborhood of the fold point, branches S_2^a and S_2^r give rise respectively to an attracting slow manifold $S_{2,\tau}^a$ and a repelling slow manifold $S_{2,\tau}^r$. Both can be described by considering y as a function of x:

$$y \equiv y_{2,\tau}(x) = \frac{B}{x} + \tau \psi(x) + O(\tau^2), \tag{20}$$

with $x \geq x_0 > 0$, $x \notin (\sqrt{B} - \delta, \sqrt{B} + \delta)$, for some $\delta > 0$ and $x_0 > 0$, and with the $\tau \to 0$ limit laying on the branches S_2^a and S_2^r. As before, invariance of slow manifolds implies $y' = \frac{dy_{2,\tau}}{dx} x'$; substituting (14) yields

$$\psi(x) = -\frac{B(x - A)}{x^2(x^2 - B)}. \tag{21}$$

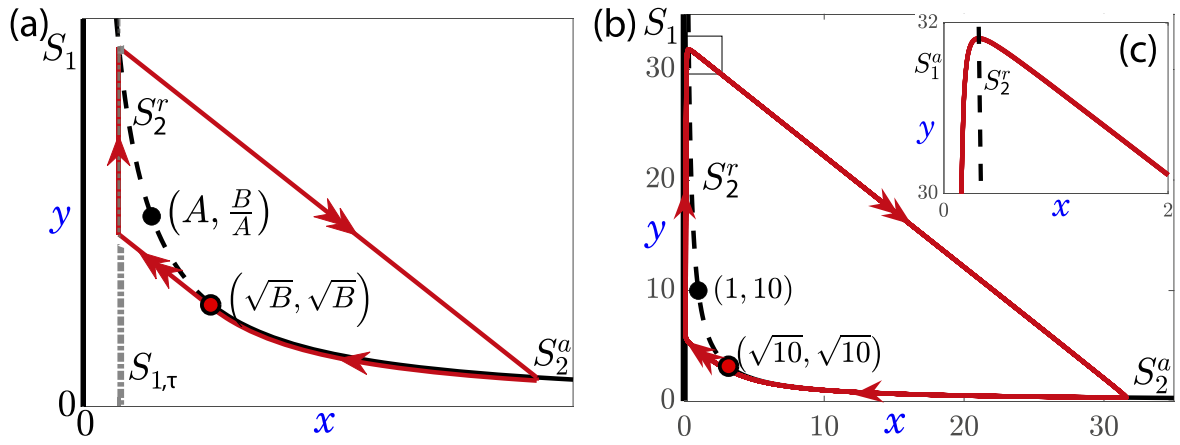

Fig. 8. (a) Critical manifold of the modified Brusselator system (14), together with the fold point (red point) and the equilibrium point of the system (in black). The slow manifold $S_{1,\tau}$ is shown as a dotted gray line, at distance $\tau\frac{A}{B}$ from S_1 (not to scale). A schematic representation of the limit cycle for small values of τ is shown in red, with single arrows indicating slow evolution and double arrows representing fast evolution. Attracting regions of the critical manifold are shown as solid black lines, and repelling regions are discontinuous black lines. (b) Numerical solution of system (14) for $\tau = 1$ (i.e. non-modified Brusselator system (3)), $A = 1$ and $B = 10$. The limit cycle shows the characteristics described in the fast–slow analysis. (c) Zoom of the squared region in (b).

Thus, the layer system on $S^a_{2,\tau}$ and $S^r_{2,\tau}$ is

$$\begin{cases} \dot{x} = -\dfrac{x^2(x-A)}{x^2-B}, \\ \dot{y} = \dfrac{B(x-A)}{x^2-B}. \end{cases} \tag{22}$$

Layer systems (19) and (22) allow us to characterize the limit cycle of the system. Starting close to S^a_2, the system evolves slowly along $S^a_{2,\tau}$ according to (22) towards the fold point. When in its neighborhood, the system enters a fast-evolution phase towards S_1, governed by (15); notice that $x+y$ is a constant along this fast evolution. The system then remains close to S_1, evolving along the slow manifold $S_{1,\tau}$ with $x = \tau\frac{A}{B}$ constant and y slowly increasing. As S_1 and S^r_2 are closer as y increases, the system eventually will reach a neighborhood of S^r_2 and will enter a new fast-evolution phase, returning to S^a_2 and restarting the cycle (see Fig. 8(a)).

The description given in terms of fast and slow evolution is valid even for non-small values of τ. Actually, in the non-modified Brusselator system (Fig. 8(b)), corresponding to $\tau = 1$, the limit cycle for an unstable equilibrium point is very similar to the characterization described above. This validation of the fast–slow analysis presented for a single Brusselator motivates the application of the singular perturbation theory to the 2-CBS model, as the resulting characterization may shed some light on interesting dynamical properties of this system.

4.2. Critical manifold of the 2-coupled Brusselator system

We present now a fast–slow analysis of the 2-CBS model. As before, let us introduce a parameter $\tau > 0$ in the 2-CBS Eqs. (4) that allows us to perform a fast–slow analysis on the system:

$$\begin{cases} x_1' = \tau(A - x_1) - Bx_1 + x_1^2 y_1 + \lambda_1(x_2 - x_1), \\ y_1' = Bx_1 - x_1^2 y_1 + \lambda_2(y_2 - y_1), \\ x_2' = \tau(A - x_2) - Bx_2 + x_2^2 y_2 + \lambda_1(x_1 - x_2), \\ y_2' = Bx_2 - x_2^2 y_2 + \lambda_2(y_1 - y_2). \end{cases} \tag{23}$$

The system shows fast–slow behavior for $0 < \tau \ll 1$, and the limit $\tau \to 0$ gives us the layer system:

$$\begin{cases} x_1' = -Bx_1 + x_1^2 y_1 + \lambda_1(x_2 - x_1), \\ y_1' = Bx_1 - x_1^2 y_1 + \lambda_2(y_2 - y_1), \\ x_2' = -Bx_2 + x_2^2 y_2 + \lambda_1(x_1 - x_2), \\ y_2' = Bx_2 - x_2^2 y_2 + \lambda_2(y_1 - y_2). \end{cases} \tag{24}$$

Equilibrium points of the layer system can be computed by solving the following set of equations:

$$\lambda_1(x_2 - x_1) = \lambda_2(y_1 - y_2) = Bx_1 - x_1^2 y_1 = -Bx_2 + x_2^2 y_2. \tag{25}$$

Solving for y_1 and y_2 from the equalities among second, third and fourth terms, and then replacing in the equality between the first and second terms give the following sets of equilibria:

1. In the general case $\lambda_1, \lambda_2 \neq 0$, the critical manifold S of the system is the union of three disjoint manifolds of equilibria:

$$S = S_A \cup S_B \cup S_C. \tag{26}$$

These manifolds are defined as follows. S_A is the set of points on the synchronization manifold Π with $x_1 = x_2 = 0$, while S_B is the set of points on Π satisfying $x_1 y_1 = x_2 y_2 = B$:

$$\begin{aligned} S_A = &\{ (x_1, y_1, x_2, y_2) \in \mathbb{R}^4 : x_1 = x_2 = 0, \\ &\qquad y_1 = y_2 = s, s > 0 \} \subset \Pi, \\ S_B = &\{ (x_1, y_1, x_2, y_2) \in \mathbb{R}^4 : x_1 = x_2 = s, \\ &\qquad y_1 = y_2 = \tfrac{B}{s}, s > 0 \} \subset \Pi. \end{aligned} \tag{27}$$

These two manifolds are the duplication of the critical manifold (16) of the single Brusselator system onto the synchronization manifold Π. Stability of each manifold can be computed through the Jacobian of system (24). In both cases, the two eigenvalues corresponding to the restriction of the flow to the (invariant) synchronization manifold Π can be obtained from local analysis in system (15): $\{0, -B\}$ along S_A and $\{0, B - s^2\}$ along S_B. It easily follows that along S_A eigenvalues in directions transverse to Π are $\{-B - 2\lambda_1, -2\lambda_2\}$, and therefore the critical manifold S_A is always attracting. On the other hand, as we already knew, S_B shows a single fold point when $s = \sqrt{B}$ and extra bifurcations can appear in directions transverse to the synchronization manifold.

Additionally, there exists a manifold S_C of equilibria transverse to the synchronization manifold Π, defined as follows:

$$\begin{aligned} S_C = \Big\{ &(x_1, y_1, x_2, y_2) \in \mathbb{R}^4 : y_1 = \tfrac{\lambda_1}{x_1} + \tfrac{\lambda_1}{x_2} + \tfrac{\lambda_1}{\lambda_2} x_2; \\ &y_2 = \tfrac{\lambda_1}{x_1} + \tfrac{\lambda_1}{x_2} + \tfrac{\lambda_1}{\lambda_2} x_1;\ x_1, x_2 > 0; \\ &\lambda_1(x_1^2 x_2^2 + \lambda_2(x_1^2 + x_2^2)) = B\lambda_2 x_1 x_2 \Big\}. \end{aligned} \tag{28}$$

Using polar coordinates, $x_1 = r\cos\theta$ and $x_2 = r\sin\theta$, the equation $\lambda_1(x_1^2 x_2^2 + \lambda_2(x_1^2 + x_2^2)) = B\lambda_2 x_1 x_2$ can be rewritten as

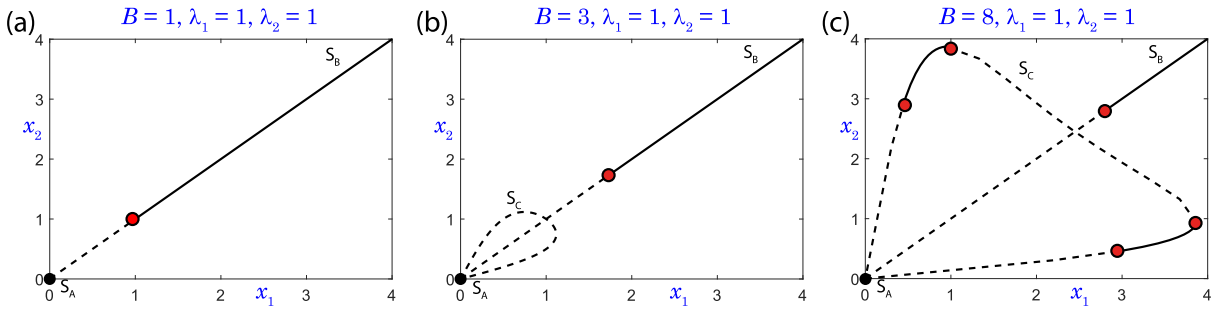

Fig. 9. Projection onto the (x_1, x_2) plane of the critical manifold (black; attracting as continuous, repelling as discontinuous) and its fold points (red points) of system (23) for the indicated values of the parameters. (a) Only S_A and S_B appear, as the equation for S_C has no solution for these parameters. Black dot on $(0, 0)$ represents the projection of S_A onto the plane; this set is attracting. Notice that all the attracting regions lay on the synchronization plane. The only possible limit cycle on the synchronization plane is the duplication of the single Brusselator limit cycle shown in Fig. 8. (b) Three sets of the critical manifold appear. However, S_C is repelling everywhere, and it does not affect the limit cycle, which is identical to the one described for panel (a). (c) If $B > 4\lambda_1$, the set S_C presents two symmetrical attracting regions. This may provide new types of orbits, as those shown in Fig. 10, that approach these regions.

follows:

$$r = \frac{1}{\sin(2\theta)}\sqrt{\frac{2B\lambda_2}{\lambda_1}\sin(2\theta) - 4\lambda_2}, \tag{29}$$

with $\sin(2\theta) > \frac{2\lambda_1}{B}$ and $B > 2\lambda_1$.
There exists no valid solution for the equation if $B \leq 2\lambda_1$. For values $2\lambda_1 < B < 4\lambda_1$, the manifold S_C is repelling everywhere. For $B \geq 4\lambda_1$, two symmetric pairs of fold points appear, generating two symmetric attracting regions. This change is shown in the plots of Fig. 9.

2. For $\lambda_1 = 0$, the critical manifold consists of 4 disjoint manifolds

$$S = S_A \cup S_B \cup S_C^1 \cup S_C^2, \tag{30}$$

with S_A, S_B the same manifolds defined in (27), and the two manifolds S_C^1 and S_C^2 defined as follows:

$$\begin{aligned} S_C^1 = \Big\{ &(x_1, y_1, x_2, y_2) \in \mathbb{R}^4 : x_1 = 0, x_2 = s, \\ &y_1 = y_2 = \frac{B}{s}, s > 0 \Big\}, \\ S_C^2 = \Big\{ &(x_1, y_1, x_2, y_2) \in \mathbb{R}^4 : x_1 = s, x_2 = 0, \\ &y_1 = y_2 = \frac{B}{s}, s > 0 \Big\}. \end{aligned} \tag{31}$$

Both manifolds S_C^1 and S_C^2 present a single fold point each, symmetric to each other. As before, S_A is attractive, but now S_B is repelling everywhere; however, the largest eigenvalue of the Jacobian on S_B is small enough to allow for trajectories to remain close to this manifold for a long time. Fig. 10 shows the critical manifold in this case, together with three different trajectories of the whole system (23) computed numerically.

3. For $\lambda_2 = 0$, the critical manifold consists of 2 disjoint manifolds:

$$S = S_A^* \cup S_B, \tag{32}$$

with S_B the same as in (27), and S_A^* the following two dimensional set:

$$S_A^* = \left\{(x_1, y_1, x_2, y_2) \in \mathbb{R}^4 : x_1 = x_2 = 0; y_1, y_2 > 0\right\}. \tag{33}$$

Notice that the intersection between S_A^* and the synchronization manifold Π is precisely the set S_A already appearing in the other cases and defined in (27).

The distribution of attracting regions of the critical manifold plotted in Fig. 9 shows that most of them lay on the synchronization plane Π. Therefore, there may exist trajectories that stay for long times close to Π, only being repelled from it to temporally evolve around the small attracting regions outside Π. This analysis thus provides a new setting in which almost synchronization can be studied. Let us start by detailing the theoretical behavior of orbits.

Assume that the system begins close to S_A. Reproducing the behavior of a single Brusselator, a slow manifold exists in a neighborhood of S_A; along it, the system evolves slowly increasing the values of y_1 and y_2. Repelling branches of S_B and S_C lay close to S_A for large values of y_1 and y_2 (see projections in Fig. 9). Thus, analogously to what occurs in the description of a single Brusselator, eventually the system will reach these repelling branches and a new fast part of dynamics will occur.

The system now may be attracted to different regions, depending on the values of the parameters. Let us consider a situation with multiple attracting regions in S_B and S_C, as in Fig. 9(c). The system may be attracted to S_B, mimicking the evolution of a single Brusselator; notice that this branch lays on the synchronization plane. However, once that the fold point is reached, analysis of the Jacobian of the system indicates that the system is repelled from the synchronization plane. Thus, it may now evolve towards the attracting regions on S_C, outside the synchronization plane. After a short period of slow evolution, the system will reach a new fold point, then evolving again towards S_A.

The described evolution is a possible behavior of the system based on the distribution of attracting and repelling regions of the critical manifold. Numerical computations support these claims. Fig. 10 shows three numerical solutions to system (23) with $A = 0.5$, $B = 1$, $\lambda_1 = 0$, $\lambda_2 = 1$ and $\tau = 0.01$. For these parameters, the critical manifold S is given by (30). Sets S_C^1 and S_C^2 present attracting regions that influence orbits starting outside of the synchronization plane Π (red and blue trajectories). As Π is invariant for the dynamics, a limit cycle also exists on it (green trajectory). All the trajectories are attracted towards S_A, which is attractive everywhere; however, as described, trajectories evolve along slow manifolds in a neighborhood of S_A and eventually are repelled from it due to the proximity of other repelling branches. The three orbits enter a fast evolution period towards S_B; this set is always repelling, although its largest eigenvalue tends asymptotically to zero and trajectories remain close to it for large times. Eventually, red and blue trajectories are repelled from S_B and move away from the synchronization plane Π; the associated eigenvector is transversal to Π, so this does not affect the green trajectory, which is only repelled when the second eigenvalue, whose eigenvector is tangent to Π, becomes positive.

Fig. 10 clearly shows how part of the trajectories stays very close to the synchronization manifold. These passages take a long time since such trajectories are following slow manifolds. Therefore, the fast–slow analysis permits to describe their dynamics. Obviously, these orbits fit in the almost synchronization concept introduced in the previous section. We calculate the β_ϵ value for the orbit in Fig. 10(a):

$$\beta_{0.1} = 1.0, \quad \beta_{0.01} = 0.9888, \quad \beta_{0.001} = 0.9881.$$

That is, the orbit is almost full synchronized but the small fraction of time that it is repelled from the vicinity of the synchronization plane Π. Therefore, we have almost synchronization, but due to the fast–slow dynamics it is practically a fully synchronized orbit.

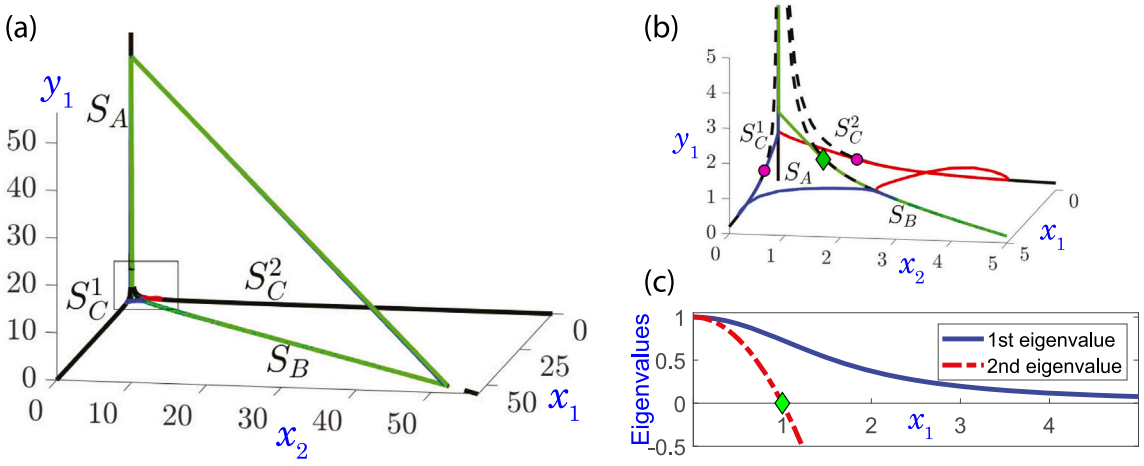

Fig. 10. Numerical computation of trajectories of system (23) for the parameter values $A = 0.5$, $B = 1$, $\lambda_1 = 0$, $\lambda_2 = 1$ and $\tau = 0.01$. **(a)** Critical manifold and three orbits (red, blue, and green). These orbits lay always close or on the synchronization plane Π, except on part of the squared region. **(b)** Enlargement of the squared region in (a), which shows how red and blue trajectories are repelled from S_B towards S_C^1 or S_C^2. The green trajectory, laying on the synchronization plane, is not affected by this, and instead is repelled from S_B when the second eigenvalue, whose eigenvector is tangent to the synchronization plane, becomes positive (green diamond-shaped point). All three trajectories are then attracted towards S_A, and eventually repelled from it, as predicted, because of the proximity of repelling branches of the critical manifold. **(c)** First two non-zero eigenvalues of the system along S_B, parametrized by x_1.

5. A coupling of three Brusselators

We have explored the dynamics of two coupled Brusselators where the rhythmic patterns and almost synchronization have been key to understanding the dynamics of the system. Coupling three Brusselators allows different patterns of (almost) synchronization to appear.

The coupling of three Brusselators is achieved by the following equations (3-CBS in the sequel), which extend the coupling introduced in (4) to an additional Brusselator system with coordinates (x_3, y_3):

$$\begin{cases} x_1' = A - (B+1)x_1 + x_1^2 y_1 + \lambda_1(x_2 - x_1) + \lambda_1(x_3 - x_1), \\ y_1' = Bx_1 - x_1^2 y_1 + \lambda_2(y_2 - y_1) + \lambda_2(y_3 - y_1), \\ x_2' = A - (B+1)x_2 + x_2^2 y_2 + \lambda_1(x_1 - x_2) + \lambda_1(x_3 - x_2), \\ y_2' = Bx_2 - x_2^2 y_2 + \lambda_2(y_1 - y_2) + \lambda_2(y_3 - y_2), \\ x_3' = A - (B+1)x_3 + x_3^2 y_3 + \lambda_1(x_1 - x_3) + \lambda_1(x_2 - x_3), \\ y_3' = Bx_3 - x_3^2 y_3 + \lambda_2(y_1 - y_3) + \lambda_2(y_2 - y_3). \end{cases} \tag{34}$$

In order to study the dynamical properties of this system, we have performed a spike-counting (SC) sweeping [43] for its orbits in a parametric region already explored in the 2-CBS, whose results are shown in Fig. 11. Each color represents the number of maxima the x_1 variable reaches until the orbit closes. A large number of maxima correlates with chaotic behavior of the orbit [9]. We can observe that the addition of a third Brusselator makes the coupled system *less* chaotic, in the sense that, compared to the case with 2 Brusselators, the chaotic region is reduced and the overall number of spikes per cycle is smaller.

In order to understand the possible patterns of synchronization of this system, we prepared an experiment similar to the one in Ref. [3] in a two parametric region studied in Ref. [35]. Given a set of initial conditions and some values for the parameters, the system is integrated with a DOPRI5 scheme with fixed step 10^{-3}. After 10^5 units of transient time we integrate for 10 units of time. As a result, we obtain 6 time series, one for each coordinate, that we distill into a 6×6 symmetric matrix to understand the almost synchronization pattern. Elements of this matrix are

$$\beta_\varepsilon^{i,j} = \frac{m(I_\varepsilon^{i,j})}{T}, \qquad I_\varepsilon^{i,j} = \{t \in [0,T] \ : \ |\xi_i(t) - \xi_j(t)| \leq \varepsilon\}, \tag{35}$$

for $i, j = 1, 2, \ldots, 6$, with coordinates $\xi = (x_1, x_2, x_3, y_1, y_2, y_3)$, a threshold $\varepsilon > 0$ and with m the Lebesgue measure on $\mathbb{R}$. These values allow us to directly measure the almost synchronization between any two coordinates. Clearly, $\beta_\varepsilon^{i,j} = \beta_\varepsilon^{j,i}$ and $\beta_\varepsilon^{i,i} = 1$. Thus, these values play a similar role in the 3-CBS to that of the β_ε fraction defined in (11), and help to characterize the almost synchronization of the system. Note that $\beta_\varepsilon^{i,j}$ extends Definition 1 of β_ε and it can be applied to any number of coupled Brusselators.

As indicated, we have arranged the $\beta_\varepsilon^{i,j}$ in a 6×6 symmetric square matrix, in which the first 3 columns and rows are associated to the x variables and the last three to the y variables; specifically, the variables of rows/columns i and $i+3$ are the variables x_i and y_i, respectively. We will call this matrix the β_ε *pattern* matrix. Fig. 12 shows the time series and the β_ε patterns with $\varepsilon = 0.05$ for three paradigmatic examples of almost synchronization. Panel (b) shows a full almost synchronization among x variables and the same for y variables. Notice that x and y variables are not in synchronization among all of them, as no term in (34) forces it; this is observed in all of the computed orbits. Panel (a) shows an orbit where x_1 and x_2 are fully almost synchronized but x_3 is only temporally almost synchronized with the others. The y variables are fully almost synchronized. Finally, panel (c) shows a less synchronized orbit. Note that the β_ε pattern matrices on the right provide a complete description of the temporal and full almost synchronization. For instance, on the case (b) of full almost synchronization of the x (and y) variables, the β_ε pattern matrix with $\varepsilon = 0.05$ is a block diagonal matrix consisting on 2 yellow blocks, that means full almost synchronization of the x variables on one side (one yellow block) and the y variables (the other yellow block). For the cases (a) and (c), the β_ε pattern matrices are block diagonal matrices but with more block elements. In case (a), as x_1 and x_2 are fully almost synchronized, but no x_3, we have 2 yellow blocks, one of the two fully almost synchronized variables, and one for the x_3. For the y variables we have just one yellow block as they are fully almost synchronized. Besides, as x_3 is only temporally almost synchronized with x_1 and x_2, we have two rectangular blocks in blue color (the fraction of time for which variables are almost synchronized is quite small, giving a low $\beta_{0.05}^{i,j}$ value). The x variables are not almost synchronized with the y variables, and so the color indicates a 0 value of $\beta_\varepsilon^{i,j}$. In case (c), we have 4 yellow blocks ((x_1, x_2), x_3, (y_1, y_2) and y_3). Note that in this case the y_3 variable is only temporally almost synchronized with (y_1, y_2), hence the green colored values.

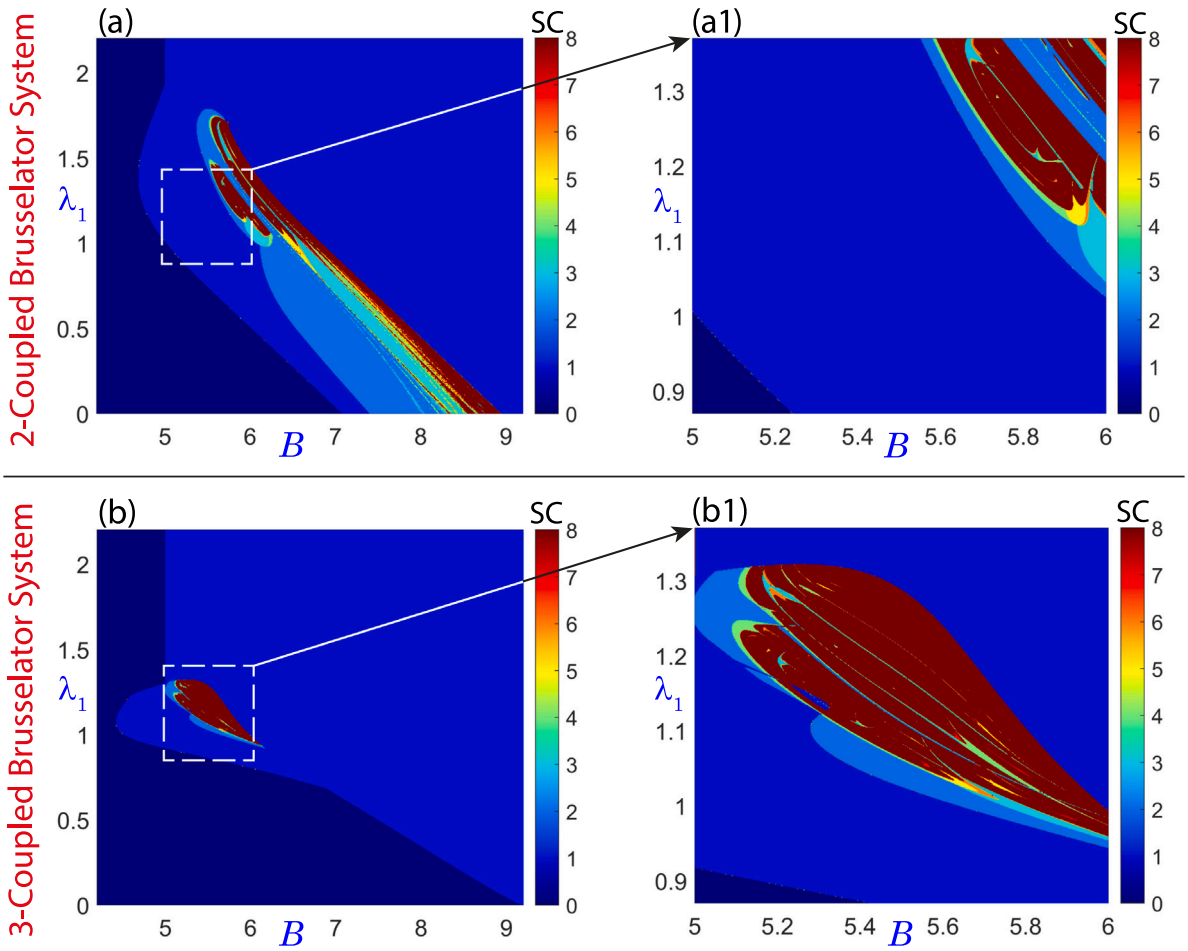

Fig. 11. Panels (a) and (a1) show the results of a spike-counting sweeping on the parametric plane (B, λ_1) for the 2-CBS. Panels (b) and (b1) reproduce these results, for the same values of the parameters, in 3-CBS case. Regions with 0 spikes correspond to stable equilibria, while regions with 1 spike indicate the existence of a stable limit cycle. In regions where the number of spikes explodes (represented as 8 spikes, although the actual number of spikes is much larger), the systems show chaotic behavior. The panels show that the general distribution of stable equilibria and stable limit cycles is similar in both systems. However, the chaotic region for the 2-CBS is larger and more complex than that for the 3-CBS. The value of the parameters used for all the figures are $A = 2$ and $\lambda_2 = 80$.

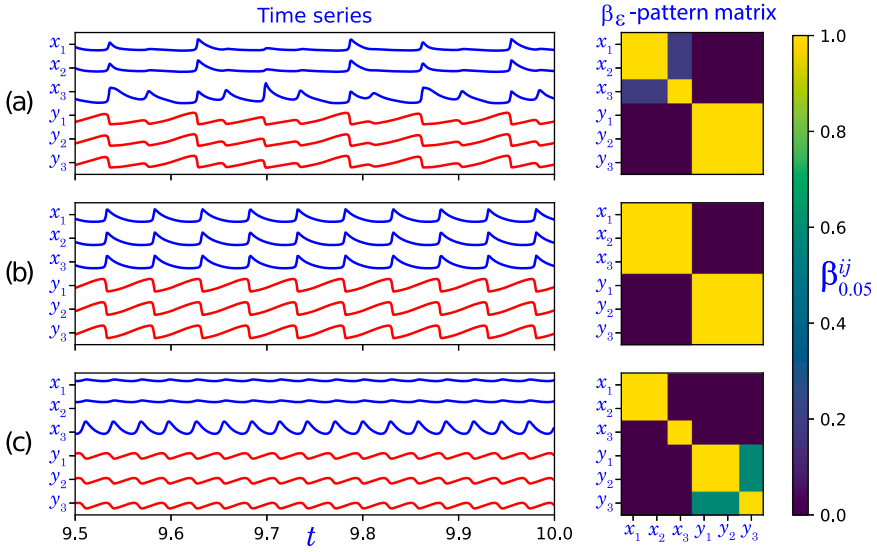

Fig. 12. In each line, the last 0.5 units of time of some orbits are shown, together with the corresponding β_ε pattern matrix for $\varepsilon = 0.05$, with elements $\beta^{ij}_{0.05}$ defined by (35). Different behaviors can be observed. Panels (a) and (c) show full almost synchronization between Brusselators 1 and 2, and different levels of temporal almost synchronization with the third Brusselator. This full almost synchronization in part of a system is a partial synchronization. Panel (b) shows full almost synchronization among all Brusselators. All values are computed for parameters values $A = 2$ and $\lambda_2 = 80$. Others parameters and initial conditions for these orbits are (a) $B = 5.89$ and $\lambda_1 = 1$, $(x_1, y_1, x_2, y_2, x_3, y_3) = (0.786027, 4.65982, 0.582159, 4.66024, 0.582159, 4.66024)$, (b) $B = 5.89$ and $\lambda_1 = 1.1$, $(x_1, y_1, x_2, y_2, x_3, y_3) = (1.92234, 2.65202, 1.92234, 2.65202, 1.92234, 2.65202)$, and (c) $B = 5.125$ and $\lambda_1 = 1$, $(x_1, y_1, x_2, y_2, x_3, y_3) = (4.76544, 1.36442, 1.37046, 1.41014, 1.37046, 1.41014)$.

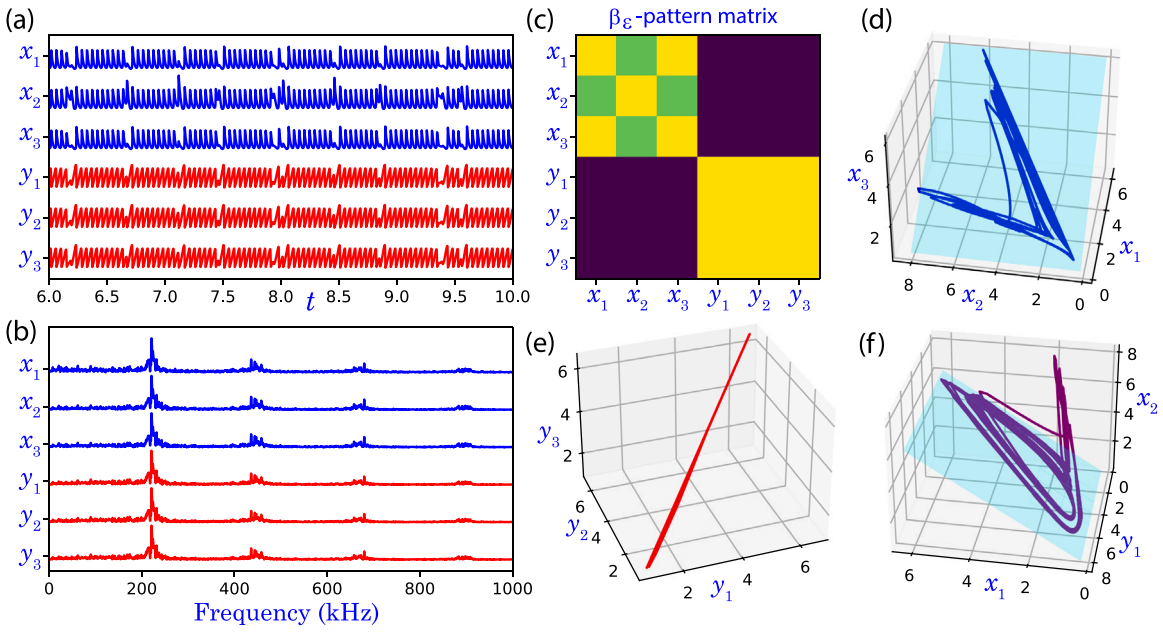

Fig. 13. Aperiodic temporal almost synchronization of the 3-CBS. Panel (a) contains the time series of the 3-CBS with $A = 2$, $B = 5.645$, $\lambda_1 = 1.2$ and $\lambda_2 = 80$, and initial conditions $(x_1, y_1, x_2, y_2, x_3, y_3) = (0.0562962962962963, 5.51, 6.706428571428571, 8.51, 2.6885714285714286, 15.635)$. Plot (b) presents the FFT of each time series, which shows a rather noisy behavior in contrast with the typical sharp spikes for a periodic orbit. However, the β_ε pattern matrix (c) suggests a strong full almost synchronization among the variables (its color map is the same as the one of Fig. 12). The 3D plots show the projection of the orbit onto different 3 dimensional spaces. The blue colored graph (d) shows the projection onto the (x_1, x_2, x_3) space; this projection is fully contained in the $x_1 = x_3$ plane (in light blue), as pointed out by the β_ε pattern. Similarly, variables y_1, y_2, y_3 are (almost) synchronized, as shown by the red plot (e), where the projection of the orbit lies on the line $y_1 = y_2 = y_3$. Finally, the purple plot (f) shows the projection onto a space of non-almost synchronized variables (x_1, x_2 and y_1); this figure shows the plane $x_1 = x_2$ in light blue for reference.

An interesting fact shown in the different patterns observed in Fig. 12 is that, among the different possible almost synchronizations, we have found the existence of partial almost synchronizations. Some of the patterns computed for the 3-CBS show that, during the collective oscillatory dynamics, some of the variables are almost synchronized, while other periodic or even chaotic dynamics occur simultaneously for other variables. In the nonlinear dynamics literature, this kind of patterns are called "chimera" states [50,51]. In fact, these are examples of the smallest chimera states [52] (illustrated in that reference for three coupled oscillators). Note that in nature this behavior is observed in numerous systems, such as the brain, mechanical systems, etc. [53,54].

Moreover, almost synchronization is possible even when the orbit is not periodic. Panel (a) of Fig. 13 presents a non-periodic temporally almost synchronized orbit and its β_ε pattern matrix for $\varepsilon = 0.05$ on plot (c). Panel (d) shows a 3D plot of the x variables. The plot lies on the plane $x_1 = x_3$ (in light blue). The 3D plot (e) shows how the orbit (mainly) lies on the line $y_1 = y_2 = y_3$. The last 3D plot (f) shows a projection of the orbit onto the (x_1, x_2, y_1) space similar to the ones in the 2-CBS (again we show the plane $x_1 = x_2$ in light blue). To address the periodicity of the orbit, we compute the FFT of each time series. The results are in the panel (b) of Fig. 13. As we can see, the diagram does not present clear peaks, a clear indication of non-periodicity. In fact, the system presents chaotic dynamics; moreover, in this situation the system exhibits chaotic almost synchronization.

To analyze the evolution of the patterns, we perform a sweep [3] on four parametric lines with $\lambda_1 \in \{1, 1.1, 1.2, 1.3\}$ in the plane of Fig. 11(b1): for 200 different values of B on each line we integrate, as above, 200 different initial conditions for each set of parameters selected through Halton sequences with $x_i \in [0.01, 10]$ and $y_i \in [0.01, 20]$, $i = 1, 2, 3$. To compare the massive amount of data, we lexicographically order the patterns, keeping the variables of the same Brusselator in the same relative position (that is, reducing it by the Σ_3-symmetry the 3-CBS presents). Hence, the largest $\beta^{ij}_{0.05}$ values appear in the upper left of the β_ε pattern matrix. In all analyzed orbits, the $\beta^{ij}_{0.05}$ values with $|i - j| \geq 3$ are zero, i.e. there is no almost synchronization between x and y coordinates (cf. Fig. 12).

Fig. 14 contains all the relevant information of the evolution of these patterns. The first column presents the almost synchronization among the x variables. Namely, red dots corresponds to the values of $\beta^{12}_{0.05}$, describing the almost synchronization of x_1 and x_2, while blue dots are the values of $\beta^{13}_{0.05}$, which describes the almost synchronization between x_1 and x_3. The second column shows the results for y variables: $\beta^{45}_{0.05}$ for y_1 and y_2, and $\beta^{46}_{0.05}$ for y_1 and y_3. Almost synchronizations between x_2 and x_3, and between y_2 and y_3, are omitted due to the existing fully synchronization between the two first Brusselators causing $\beta^{13}_{0.05} = \beta^{23}_{0.05}$ and $\beta^{46}_{0.05} = \beta^{56}_{0.05}$. Panels in each row of the figure show the evolution of the patterns along the selected lines: as before, the results are computed after the integration of 200 orbits for each chosen value of B in the interval $[5, 6]$. Since we have reordered the Brusselators for better comparison, coordinates x_1 and x_2, as well as y_1 and y_2, are fully synchronized for any $\lambda_1 \in \{1, 1.1, 1.2, 1.3\}$ (red dots in each of the scatter plots). For reference, below each panel, the results of the spike-counting presented in Fig. 11 are shown in a strip of the indicated values of λ_1; the maximum value of λ_1 on each strip corresponds to the results of the panel above it.

In all cases shown in Fig. 14, for $B = 5$ the system exhibits chimeras [50,51], as the two first Brusselators are fully synchronized, while the third is not (see Fig. 12(c)). This chimera behavior remains almost the same, with $\beta^{46}_{0.05}$ slowly increasing, until B reaches the spike-adding region, where abrupt increases on $\beta^{13}_{0.05}$ and $\beta^{46}_{0.05}$ happen. In this region, characterized by chaotic behavior, different patterns arise for the same value of B. In the non-chaotic regions we see that this noisy behavior disappears. This can be seen in panels on the first column for $\lambda_1 = 1.1$ and 1.2. Finally, increasing B and leaving the chaotic region we see full synchronization like Fig. 12(b).

In order to understand the periodicity of the orbits analyzed in Fig. 14, we have computed the FFT for the time series normalized to values in $[0, 1]$. Then, for each variable, we compute the ratio of frequencies which have amplitude at least 10% of the main frequency (maximal amplitude), and we assign the maximum of these values to the orbit. Near-zero values indicate periodicity, while other values suggest that the orbits are not periodic. This information is included, as

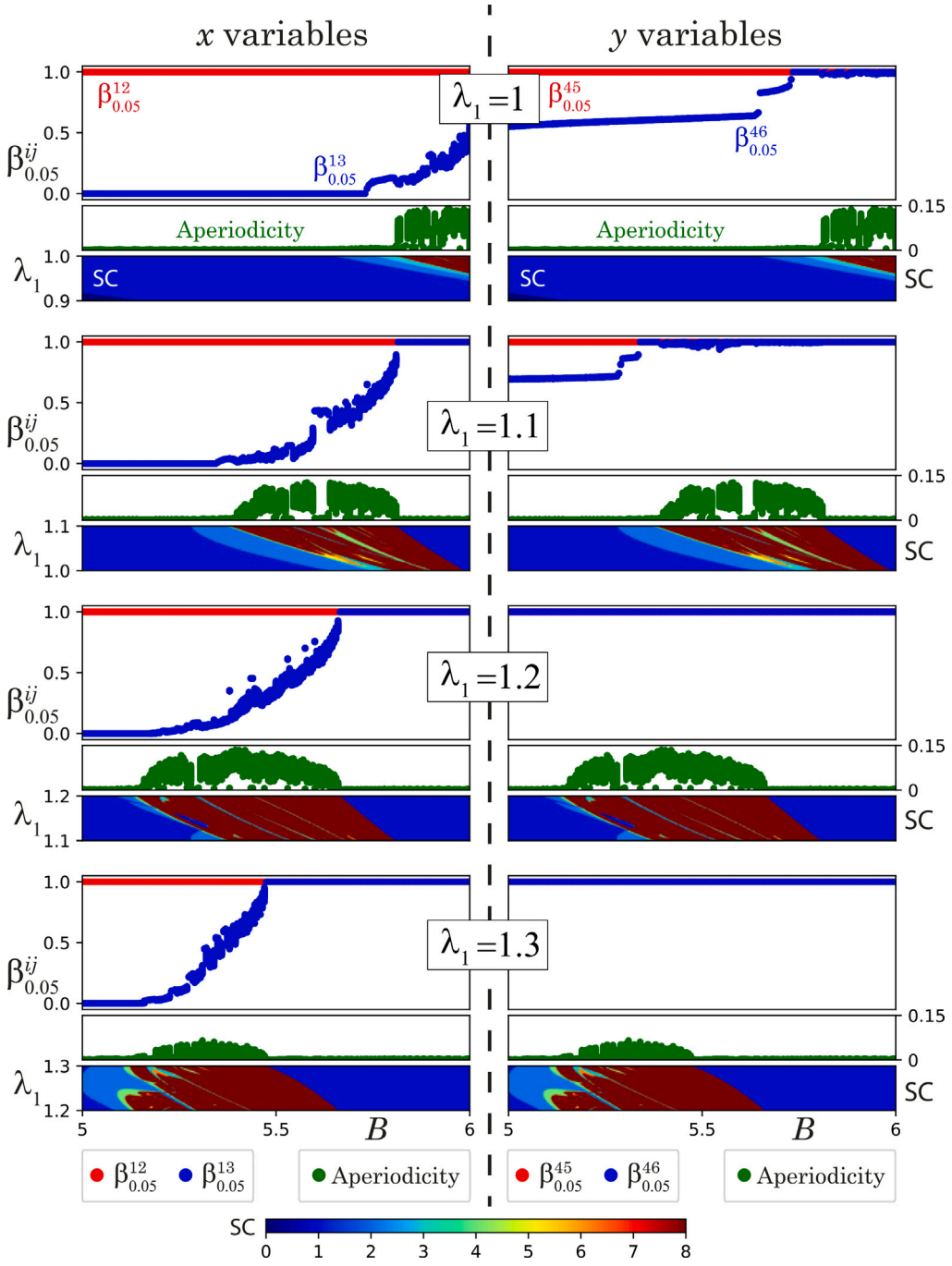

Fig. 14. Temporal almost synchronization and full synchronization of the variables of the 3-CBS for different values of B and λ_1 ($\lambda_1 = 1$, 1.1, 1.2 and 1.3). Panels shown temporal almost synchronization between x variables and between y variables as indicated, represented by $\beta^{ij}_{0.05}$ as defined in (35). Colored stripes reproduce the spike-counting results already shown in Fig. 11, with the larger λ_1 value in each strip corresponding to the panel above it. Aperiodicity of orbits, related to large numbers of spikes and chaotic behavior, is also shown. Panels show the evolution of the temporal almost synchronization between different variables: temporal almost synchronization occurs when any $\beta^{ij}_{0.05} \neq 0$, full almost synchronization is achieved if all $\beta^{ij}_{0.05} = 1$, and chimeras are found when only some $\beta^{ij}_{0.05} = 1$. Each $\beta^{ij}_{0.05}$ is computed from the integration of 200 orbits with different initial conditions, as described in the text. Parameters for the simulations are $A = 2$ and $\lambda_2 = 80$.

green dots, in Fig. 14. As we can see there, the non-periodicity appears, as expected, on the chaotic areas. Moreover, the aperiodicity is related to the modification of the patterns, as the almost synchronization increases for larger values of B in all panels.

A detailed analysis of the results for $\lambda_1 = 1.1$ are presented in Fig. 15. The left panel shows the temporal almost synchronization between x_1 and x_3 ($\beta^{13}_{0.05}$, in blue), and y_1 and y_3 ($\beta^{46}_{0.05}$, in red), already shown in Fig. 14; other $\beta^{ij}_{0.05}$ values are omitted due to the existing full synchronization between x_1 and x_2, and between y_1 and y_2. For selected values of B, namely, 5.1, 5.315, 5.375, 5.615, 5.755 and 5.95, and fixed initial conditions in all cases, right panels show the time series of all the coordinates for the orbits. These time series clearly show the described behavior of the system, from temporal almost synchronization for lower

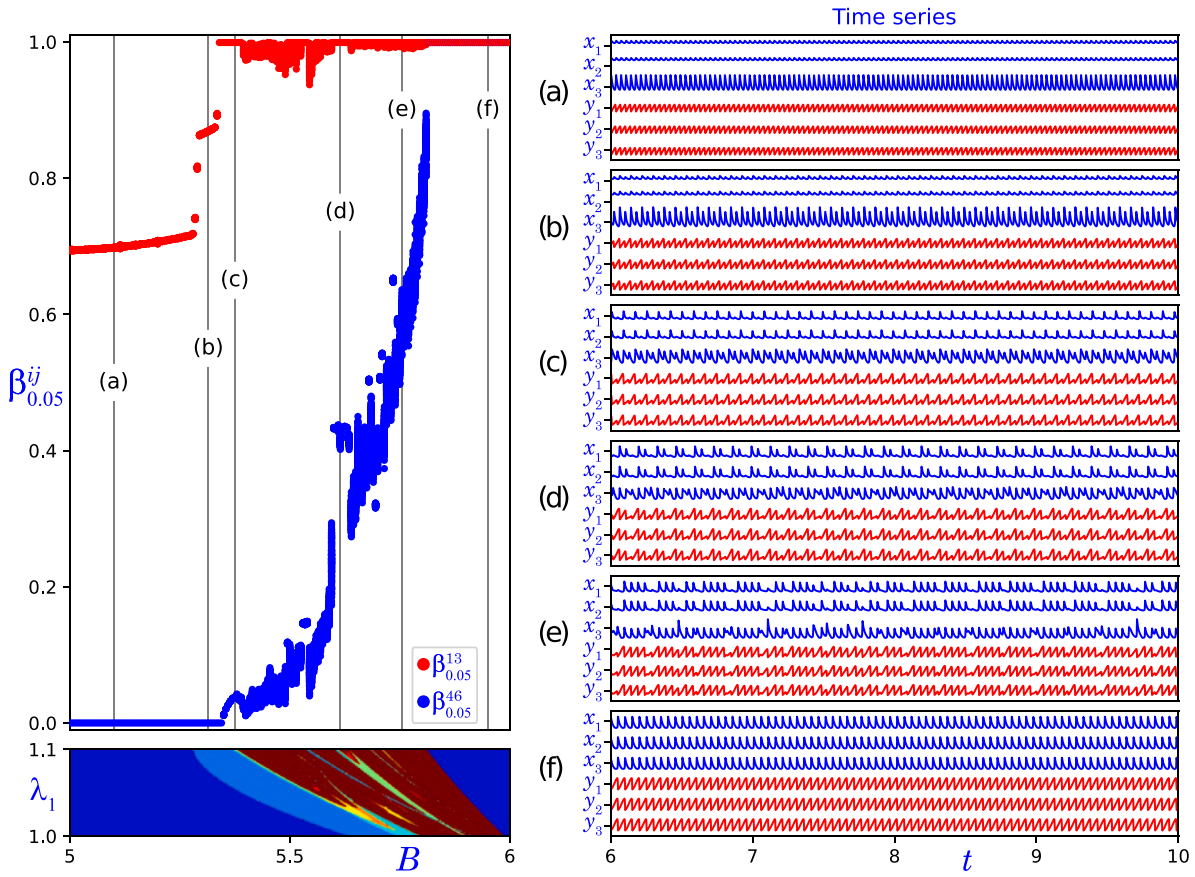

Fig. 15. Detailed analysis of six different orbits from Fig. 14, $\lambda_1 = 1.1$ case. All orbits are computed with identical initial conditions, with $A = 2$, $\lambda_1 = 1.1$, $\lambda_2 = 80$, and (a) $B = 5.1$, (b) $B = 5.315$, (c) $B = 5.375$, (d) $B = 5.615$, (e) $B = 5.755$, (f) $B = 5.95$. On the left panel, almost synchronization between coordinates x_1 and x_3, and between y_1 and y_3, is represented by $\beta^{13}_{0.05}$ and $\beta^{46}_{0.05}$, respectively; below it, a strip of Fig. 11 shows the results of the spike-counting sweeping. Right panels show the time series of all the variables for the chosen orbits. The different almost synchronization phenomena can be clearly seen. Orbits from (a) to (e) show increasing levels of almost synchronization and chimera behavior, with coordinates x_3 and y_3 approaching synchronization with the other variables when the system enters the chaotic region. Orbit (f), outside of the chaotic region, shows full synchronization among all three Brusselators.

values of B to full synchronization among x and among y variables for $B = 5.95$.

6. Conclusions

In this paper, we have characterized some synchronization properties of coupled Brusselator systems (CBS). While it is clear from the equations of the model that full synchronization of the Brusselators is possible and, indeed, stable under the coupled dynamics, a detailed numerical analysis of the system shows the emergence of temporal almost synchronization, a state in which the Brusselators are approximately synchronized only in a fraction of the total orbit of the CBS.

Our study focuses on some characterizations of the temporal almost synchronization phenomena in the 2-CBS. Based on a detailed study of codimension-two Hopf–pitchfork bifurcations appearing in the 2-CBS, we have determined the appropriate parameter regions on which they may occur. A numerical analysis shows the existence of dome-like periodic orbits exhibiting temporal almost synchronization, as the Brusselators are almost synchronized for up to 70% of the period of the orbit. The existence of these orbits is predicted theoretically from an analysis of stable and unstable manifolds of the equilibria and limit cycles of the system, and computed numerically.

Temporal almost synchronizations are also shown to appear in a fast–slow regime. Theoretical results and computations of critical manifolds of CBS characterize trajectories lying close to the synchronization plane for large times. Numerical computations of β_ϵ in this regime show large values close to the full synchronization state.

The above results motivate the analysis of almost synchronization in the 3-CBS. This system presents more complex behavior, as not only almost synchronization occurs, but also only part of the full system achieves synchronization. Thus, we prove numerically the existence of chimeras in the 3-CBS, as state of the system where only 2 out of 3 Brusselators are synchronized. A detailed analysis shows how variations in the parameters allow the system to change from chimera states and partial synchronization to collective synchronization among all 3 Brusselators.

Moreover, we have introduced some techniques based on the concept of temporal almost synchronization, the β_ϵ pattern matrix, that may help in the study of small coupled systems.

CRediT authorship contribution statement

Ana Mayora-Cebollero: Writing – original draft, Visualization, Software, Investigation. **Jorge A. Jover-Galtier:** Writing – review & editing, Writing – original draft, Formal analysis. **Fátima Drubi:** Writing – original draft, Methodology, Investigation, Formal analysis, Conceptualization. **Santiago Ibáñez:** Writing – review & editing, Writing – original draft, Methodology, Investigation, Funding acquisition, Formal analysis, Conceptualization. **Álvaro Lozano:** Writing – original draft, Visualization, Software, Investigation. **Carmen Mayora-Cebollero:** Writing – original draft, Visualization, Software, Investigation. **Roberto Barrio:** Writing – review & editing, Writing – original draft, Visualization, Supervision, Project administration, Methodology, Investigation, Funding acquisition.

Declaration of competing interest

The authors declare that they have no known competing financial interests or personal relationships that could have appeared to influence the work reported in this paper.

Acknowledgments

Funding

This work was supported by the Agencia Estatal de Investigación, Spain [grant numbers PID2021-122961NB-I00, PID2020-113052GB-I00]; the European Regional Development Fund and the Diputación General de Aragón [grant number E24-23R].

Appendix A. Hopf–pitchfork bifurcations

Let X_μ be a C^∞ family of 3-dimensional vector fields, with $\mu = (\mu_1, \mu_2) \in \mathbb{R}^2$, such that $X_\mu(0) = 0$ for all μ, and $DX_0(0)$ has eigenvalues $\{\pm\omega i, 0\}$, with $\omega > 0$. Assuming that the family is invariant under a reflection $(x, y, z) \to (x, y, -z)$, we say that X_μ is an unfolding of an HP singularity. It follows from Refs. [24,55,56] that X_μ can be written in the following normal form:

$$\begin{cases} x' = \mu_1 x - \omega y + x F_\mu\left(x^2+y^2, z^2\right) \\ \qquad - y\widetilde{F}_\mu\left(x^2+y^2, z^2\right) + \phi_1(x, y, z, \mu_1, \mu_2), \\ y' = \omega x + \mu_1 y + x\widetilde{F}_\mu\left(x^2+y^2, z^2\right) \\ \qquad + y F_\mu\left(x^2+y^2, z^2\right) + \phi_2(x, y, z, \mu_1, \mu_2), \\ z' = \mu_2 z + z G_\mu\left(x^2+y^2, z^2\right) + \phi_3(x, y, z, \mu_1, \mu_2), \end{cases} \tag{A.1}$$

where F_μ, $\widetilde{F}_\mu$ and G_μ are polynomial functions in two variables of degree $d \le N$ (value N can be arbitrarily large) vanishing at $(0, 0)$, and $\phi_i = O(|(x, y, z)|^{2N+2})$ for $i = 1, 2, 3$. It should be noticed that the $\mathbb{Z}_2$-symmetry is preserved under reduction to normal form. By truncation at order $2N + 1$, we get a family which is invariant under rotations around the z-axis.

The first step to study the system (A.1) is to consider the truncated normal form and to introduce cylindrical coordinates (r, z, θ), which gives as a result the following system of equations:

$$\begin{cases} r' = r\left(\mu_1 + F_\mu\left(r^2, z^2\right)\right), \\ z' = z\left(\mu_2 + G_\mu\left(r^2, z^2\right)\right), \\ \theta' = \omega + \widetilde{F}_\mu(r^2, z^2). \end{cases} \tag{A.2}$$

Since $\theta' > 0$ in a neighborhood of the origin, time can be rescaled to get $\theta' = 1$. Hence, the study of the truncated normal form reduces to the case of a family of planar vector fields in coordinates (r, z)

$$\begin{cases} r' = r\left(\mu_1 + A_\mu^{11} r^2 + A_\mu^{12} z^2 + B_\mu^{11} r^4 \right. \\ \qquad \left. + B_\mu^{12} r^2 z^2 + B_\mu^{13} z^4 + O(|(r^2, z^2)|^3)\right), \\ z' = z\left(\mu_2 + A_\mu^{21} r^2 + A_\mu^{22} z^2 + B_\mu^{21} r^4 \right. \\ \qquad \left. + B_\mu^{22} r^2 z^2 + B_\mu^{23} z^4 + O(|(r^2, z^2)|^3)\right), \end{cases} \tag{A.3}$$

where F_μ and G_μ have been expanded up to order two. Codimension-two HP bifurcations are characterized by the conditions

$$A_0^{11} A_0^{12} A_0^{21} A_0^{22} \neq 0, \qquad A_0^{11} A_0^{22} - A_0^{12} A_0^{21} \neq 0. \tag{A.4}$$

Up to time reversal, we can assume that A_0^{11} is either positive or negative and, following Ref. [40], we assume that $A_0^{11} < 0$. Coefficients A_μ^{11} and A_μ^{22} can be normalized to get $A_\mu^{11} = -1$ and $A_\mu^{22} = \pm 1$. Finally, a hypernormal form can be obtained that allows to simplify fifth-order terms to get:

$$\begin{cases} r' = r\left(\mu_1 - r^2 + A_\mu^{12} z^2 + O(|(r^2, z^2)|^3)\right), \\ z' = z\left(\mu_2 + A_\mu^{21} r^2 + A_\mu^{22} z^2 + B_\mu^{23} z^4 + O(|(r^2, z^2)|^3)\right), \end{cases} \tag{A.5}$$

where we have preserved notation for variables, parameters and coefficients.

There are twelve different HP singularities, as classified by Guckenheimer and Holmes [24]. Classification depends on the signs of A_0^{12}, A_0^{21}, A_0^{22} and $\Delta = A_0^{22} - A_0^{12} A_0^{21}$ (see Ref. [24, Table 7.5.2] or Ref. [40, Table 1]). Most of the bifurcation diagrams are determined only by the terms up to order three, but there are some cases for which the additional generic condition $B_0^{23} \neq 0$ is required. In this paper we are only interested in Case VIa which is characterized by the conditions:

$$A_0^{12} < 0, \quad A_0^{21} > 0, \quad 1 + A_0^{12} A_0^{21} < 0, \quad B_0^{23} < 0. \tag{A.6}$$

The bifurcation diagram for the truncated normal form (A.5) is shown in Fig. A.16. The list of codimension-one bifurcations is the following:

- $\mathtt{P}_1^-$ Pitchfork bifurcation. Moving from Region 1 to Region 2, an attractor emerges on the r-axis and the origin changes into a saddle node. For family (A.2), $\mathtt{P}_1^-$ corresponds to a *Hopf bifurcation* on $z = 0$.
- $\mathtt{P}_3$ Pitchfork bifurcation (transverse to r-axis). Moving from Region 2 to Region 3, an attractor (red point) emerges in the interior of the first quadrant whereas the equilibrium point on the r-axis changes into a saddle node. For family (A.2), $\mathtt{P}_3$ is a *curve of branch points of periodic orbits*, and an attracting periodic orbit emerges on the region $z > 0$.
- $\mathtt{H}$ Hopf bifurcation. Moving from Region 3 to Region 4, an attracting limit cycle emerges whereas the equilibrium point in the interior of the first quadrant changes into a repeller. For family (A.2), $\mathtt{H}$ corresponds to a *Neimark–Sacker bifurcation*, and an attracting 2-torus emerges on the region $z > 0$.
- $\mathtt{HC}$ Heteroclinic cycle. Moving from Region 4 to Region 5, the periodic orbit disappears through a heteroclinic cycle (magenta color in the phase-portrait for $\mathtt{HC}$). For parameter values on Region 5, one of the branches of the unstable manifold of the saddle node on the r-axis is contained in the basin of attraction of the limit cycle. For parameter values on Region 6, one of the branches of the stable manifold of the saddle node on the z-axis is contained in the basin of repulsion of the equilibrium point in the first quadrant. The corresponding bifurcation in family (A.2) is described below.
- $\mathtt{P}_4$ Pitchfork bifurcation (transverse to z-axis). Moving from Region 5 to Region 6, the repelling equilibrium point contained in the first quadrant collapses with the saddle node on the z-axis which changes into a repeller. For family (A.2), $\mathtt{P}_4$ corresponds to a *Hopf bifurcation* (transverse to the z-axis).
- $\mathtt{P}_2^+$ Pitchfork bifurcation. Moving from Region 6 to Region 7, the repelling equilibrium on the z-axis collapses with the origin which changes into a saddle node. For family (A.2), $\mathtt{P}_2^+$ also corresponds to a *pitchfork bifurcation*.
- $\mathtt{P}_1^+$ Pitchfork bifurcation. Moving from Region 7 to Region 8, a saddle node on the r-axis collapses with the repeller at the origin that changes into a saddle node. For family (A.2), $\mathtt{P}_1^+$ corresponds to a *Hopf bifurcation* on $z = 0$.
- $\mathtt{P}_2^-$ Pitchfork bifurcation. Moving from Region 8 to Region 1, a saddle node emerges on the z-axis and the origin changes into an attractor. For family (A.2), $\mathtt{P}_2^-$ also corresponds to a *pitchfork bifurcation*.

For parameter values on $\mathtt{HC}$, family (A.2) exhibits an heteroclinic cycle configuration consisting of:

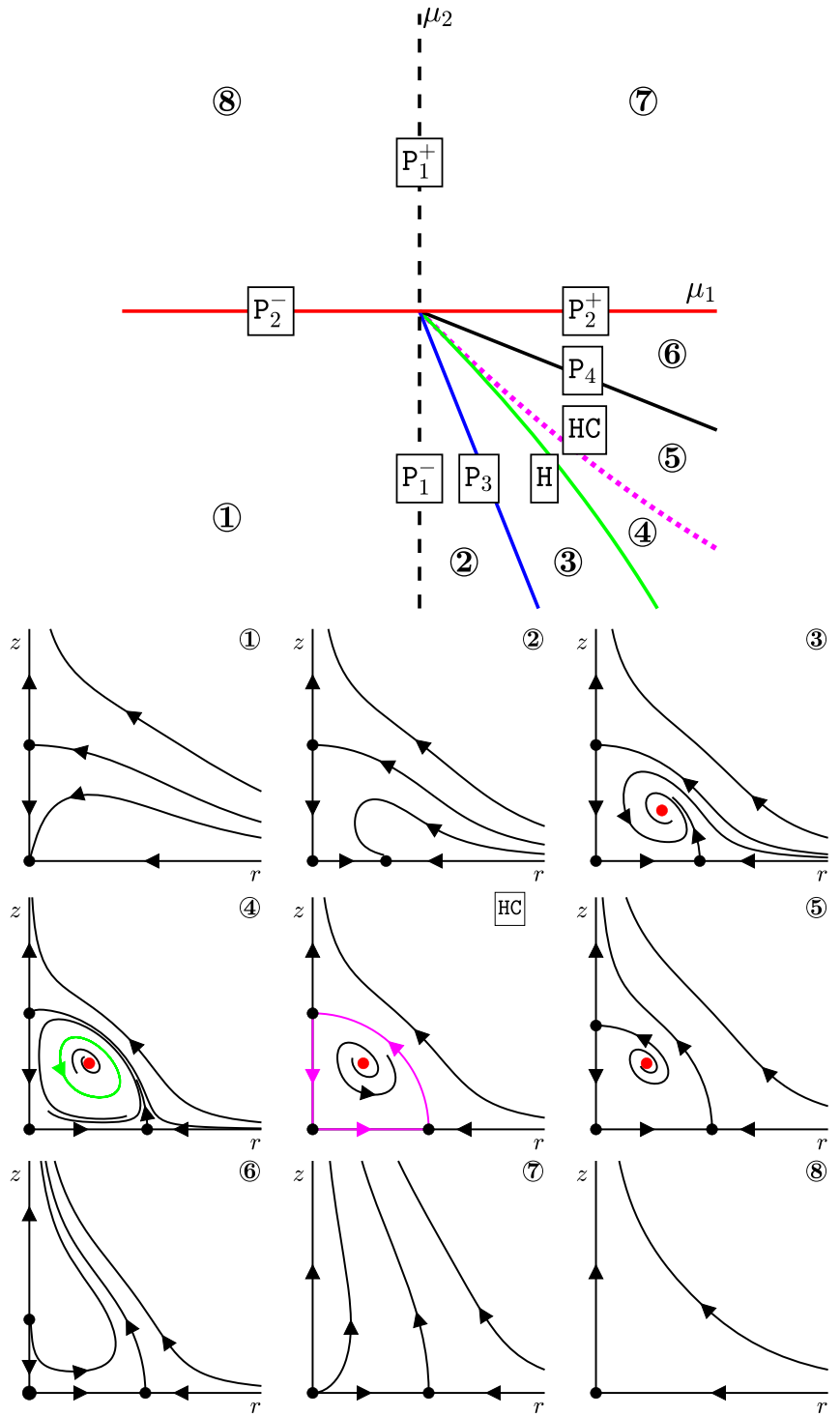

Fig. A.16. Bifurcation diagram corresponding to Case VIa in the classification by Guckenheimer and Holmes provided in Ref. [24]. Bifurcation curves $P_1^{\pm}$, $P_2^{\pm}$, P_3, P_4, H and HC split the parameter space in eight regions; a representative phase-portrait is provided for each one of them. Moreover, a phase-portrait is given to illustrate the bifurcation that happens along the line HC, the creation of a heteroclinic cycle.

1. a saddle-focus equilibrium point at the origin,
2. a saddle-focus equilibrium point on the z-axis,
3. a saddle-type limit cycle contained on the invariant plane $z = 0$,
4. a connection along the 1-dimensional invariant manifolds of the equilibrium points, contained in the z-axis,
5. the (2-dimensional) unstable manifold of the origin which is contained in the (2-dimensional) stable manifold of the limit cycle (these manifolds are contained in the plane $z = 0$),
6. the (2-dimensional) unstable manifold of the limit cycle which is coincident with the (2-dimensional) stable manifold of the saddle-focus equilibrium point on the z-axis.

According to Refs. [24,57], the full family (A.1) will exhibit all the codimension-one bifurcation curves that family (A.2) displays, except HC. Indeed, the connection along the 1-dimensional invariant manifolds of the equilibrium points contained in the z-axis will disappear if higher order terms are added. The 2-dimensional unstable manifold of the

limit cycle contained in the invariant plane $z = 0$ and the 2-dimensional stable manifold of the equilibrium point outside the invariant plane are no longer coincident. Instead, these two manifolds will intersect transversely. Hence, adding higher order terms there is a chance for the appearance of Shilnikov homoclinic orbits and chaotic behaviors. On the other hand, the dynamics on the torus in the full system will be different from that in the truncated system.

Appendix B. Supplementary data

Supplementary material related to this article can be found online at https://doi.org/10.1016/j.physd.2024.134457.

Data availability

Data will be made available on request.

References

[1] A.L. Hodgkin, A.F. Huxley, A quantitative description of membrane current and its application to conduction and excitation in nerve, J. Physiol. 117 (1952) 500–544, http://dx.doi.org/10.1113/jphysiol.1952.sp004764.

[2] Á. Lozano, M. Rodriguez, R. Barrio, Control strategies of 3-cell central pattern generator via global stimuli, Sci. Rep. UK 6 (2016) 23622, http://dx.doi.org/10.1038/srep23622.

[3] R. Barrio, Á. Lozano, M. Rodríguez, S. Serrano, Numerical detection of patterns in CPGs: Gait patterns in insect movement, Commun. Nonlinear Sci. 82 (2020) 105047, http://dx.doi.org/10.1016/j.cnsns.2019.105047.

[4] R. Barrio, Á. Lozano, M.Á. Martínez, M. Rodríguez, S. Serrano, Routes to tripod gait movement in hexapods, Neurocomputing 461 (2021) 679–695, http://dx.doi.org/10.1016/j.neucom.2020.06.151.

[5] E. Montbrió, D. Pazó, A. Roxin, Macroscopic description for networks of spiking neurons, Phys. Rev. X 5 (2015) 021028, http://dx.doi.org/10.1103/PhysRevX.5.021028.

[6] H. Taher, D. Avitabile, M. Desroches, Bursting in a next generation neural mass model with synaptic dynamics: a slow–fast approach, Nonlinear Dynam. 108 (2022) 4261–4285, http://dx.doi.org/10.1007/s11071-022-07406-6.

[7] A.M. Turing, The chemical basis of morphogenesis, Philos. Trans. R. Soc. London [Biol] 237 (641) (1952) 37–72, http://dx.doi.org/10.1007/BF02459572.

[8] J.C. Alexander, Spontaneous oscillations in two 2-component cells coupled by diffusion, J. Math. Biol. 23 (2) (1986) 205–219, http://dx.doi.org/10.1007/BF00276957.

[9] F. Drubi, A. Mayora-Cebollero, C. Mayora-Cebollero, S. Ibáñez, J.A. Jover-Galtier, A. Lozano, L. Pérez, R. Barrio, Connecting chaotic regions in the coupled brusselator system, Chaos Solitons Fractals 169 (2023) 113240, http://dx.doi.org/10.1016/j.chaos.2023.113240.

[10] S. Smale, A mathematical model of two cells via Turing's equation, in: J.E. Marsden, M. McCracken (Eds.), The Hopf Bifurcation and Its Applications, Springer, New York, http://dx.doi.org/10.1007/978-1-4612-6374-6_24.

[11] S.H. Strogatz, From Kuramoto to Crawford: exploring the onset of synchronization in populations of coupled oscillators, Phys. D 143 (1) (2000) 1–20, http://dx.doi.org/10.1016/S0167-2789(00)00094-4.

[12] V.N. Belykh, I.V. Belykh, M. Hasler, Connection graph stability method for synchronized coupled chaotic systems, Phys. D 195 (1) (2004) 159–187, http://dx.doi.org/10.1016/j.physd.2004.03.012.

[13] L.M. Pecora, T.L. Carroll, Master stability functions for synchronized coupled systems, Phys. Rev. Lett. 80 (1998) 2109–2112, http://dx.doi.org/10.1103/PhysRevLett.80.2109.

[14] A. Pikovsky, M. Rosenblum, J. Kurths, Synchronization: A Universal Concept in Nonlinear Sciences, Cambridge University Press, ISBN: 978-0-5215-3352-2, 2001.

[15] A. Pogromsky, H. Nijmeijer, Cooperative oscillatory behavior of mutually coupled dynamical systems, IEEE T Circuits-I 48 (2) (2001) 152–162, http://dx.doi.org/10.1109/81.904879.

[16] A.Y. Pogromsky, A partial synchronization theorem, Chaos 18 (3) (2008) 037107, http://dx.doi.org/10.1063/1.2959145.

[17] R. Femat, G. Solis-Perales, On the chaos synchronization phenomena, Phys. Lett. A 262 (1) (1999) 50–60, http://dx.doi.org/10.1016/S0375-9601(99)00667-2.

[18] M.G. Rosenblum, A.S. Pikovsky, J. Kurths, Phase synchronization of chaotic oscillators, Phys. Rev. Lett. 76 (1996) 1804–1807, http://dx.doi.org/10.1103/PhysRevLett.76.1804.

[19] N.F. Rulkov, M.M. Sushchik, L.S. Tsimring, H.D.I. Abarbanel, Generalized synchronization of chaos in directionally coupled chaotic systems, Phys. Rev. E 51 (1995) 980–994, http://dx.doi.org/10.1103/PhysRevE.51.980.

[20] M.S. Baptista, H.-P. Ren, J.C.M. Swarts, R. Carareto, H. Nijmeijer, C. Grebogi, Collective almost synchronisation in complex networks, PLOS ONE 7 (11) (2012) 1–11, http://dx.doi.org/10.1371/journal.pone.0048118.

[21] M.G. Pedersen, M. Brøns, M.P. Sørensen, Amplitude-modulated spiking as a novel route to bursting: Coupling-induced mixed-mode oscillations by symmetry breaking, Chaos 32 (1) (2022) 013121, http://dx.doi.org/10.1063/5.0072497.

[22] K.U. Kristiansen, M.G. Pedersen, Mixed-mode oscillations in coupled Fitzhugh–Nagumo oscillators: Blow-up analysis of cusped singularities, SIAM J. Appl. Dyn. Syst. 22 (2) (2023) 1383–1422, http://dx.doi.org/10.1137/22M1480495.

[23] W. Horsthemke, P.K. Moore, Turing instability in inhomogeneous arrays of diffusively coupled reactors, J. Phys. Chem. A 108 (12) (2004) 2225–2231, http://dx.doi.org/10.1021/jp037029k.

[24] J. Guckenheimer, P. Holmes, Nonlinear Oscillations, Dynamical Systems, and Bifurcations of Vector Fields, Springer, New York, ISBN: 978-1-4612-1140-2, 2013.

[25] Y.A. Kuznetsov, Elements of Applied Bifurcation Theory, third ed., Springer-Verlag, New York, ISBN: 978-1-4757-3978-7, 2004.

[26] G. Nicolis, I. Prigogine, Self-organization in nonequilibrium systems, in: From Dissipative Structures To Order Through Fluctuations, J. Wiley & Sons, New York, ISBN: 978-0-4710-2401-9, 1977.

[27] T.J. Kaper, An introduction to geometric methods and dynamical systems theory for singular perturbation problems, Proc. Symp. Appl. Math. 56 (1999) 85–131, http://dx.doi.org/10.1090/psapm/056.

[28] C. Kuehn, Multiple Time Scale Dynamics, Springer, Cham, ISBN: 978-3-319-12316-5, 2015.

[29] M. Wechselberger, Geometric Singular Perturbation Theory beyond the Standard Form, Springer, Cham, ISBN: 978-3-030-36399-4, 2020.

[30] R. Barrio, M.Á. Martínez, L. Pérez, E. Pueyo, Bifurcations and slow-fast analysis in a cardiac cell model for investigation of early afterdepolarizations, Math. 8 (6) (2020) 880, http://dx.doi.org/10.3390/math8060880.

[31] R. Bertram, J.E. Rubin, Multi-timescale systems and fast-slow analysis, Math. Biosci. 287 (2017) 105–121, http://dx.doi.org/10.1016/j.mbs.2016.07.003.

[32] T. Vo, R. Bertram, Why pacing frequency affects the production of early afterdepolarizations in cardiomyocytes: An explanation revealed by slow-fast analysis of a minimal model, Phys. Rev. E 99 (2019) 052205, http://dx.doi.org/10.1103/PhysRevE.99.052205.

[33] J.M. Ginoux, J. Llibre, Canards existence in FitzHugh–Nagumo and Hodgkin–Huxley neuronal models, Math. Probl. Eng. 2015 (2015) 342010, http://dx.doi.org/10.1155/2015/342010.

[34] M. Desroches, J. Guckenheimer, B. Krauskopf, C. Kuehn, H.M. Osinga, M. Wechselberger, Mixed-mode oscillations with multiple time scales, SIAM Rev. 54 (2) (2012) 211–288, http://dx.doi.org/10.1137/100791233.

[35] I. Schreiber, M. Marek, Strange attractors in coupled reaction–diffusion cells, Phys. D 5 (2) (1982) 258–272, http://dx.doi.org/10.1016/0167-2789(82)90021-5.

[36] J.C. Alexander, A period-doubling bubble in the dynamics of two coupled oscillators, in: H.G. Othmer (Ed.), Nonlinear Oscillations in Biology and Chemistry, Springer, Berlin, Heidelberg, ISBN: 978-3-642-93318-9, 1986, pp. 208–220.

[37] E.I. Volkov, V.A. Romanov, Bifurcations in the system of two identical diffusively coupled brusselators, Phys. Scr. 51 (1) (1995) 19, http://dx.doi.org/10.1088/0031-8949/51/1/004.

[38] F. Drubi, S. Ibáñez, J.A. Rodríguez, Coupling leads to chaos, J. Differential Equations 239 (2) (2007) 371–385, http://dx.doi.org/10.1016/j.jde.2007.05.024.

[39] F. Drubi, S. Ibáñez, J.A. Rodríguez, Singularities and chaos in coupled systems, Bull. Belg. Math. Soc. Simon Stevin 15 (5) (2008) 797–808, http://dx.doi.org/10.36045/bbms/1228486408.

[40] F. Drubi, S. Ibáñez, J.A. Rodríguez, Hopf-pitchfork singularities in coupled systems, Phys. D 240 (9) (2011) 825–840, http://dx.doi.org/10.1016/j.physd.2010.12.013.

[41] A. Dhooge, W. Govaerts, Y.A. Kuznetsov, H.G. Meijer, B. Sautois, New features of the software MatCont for bifurcation analysis of dynamical systems, Math. Comput. Model. Dyn. Syst. 14 (2) (2008) 147–175, http://dx.doi.org/10.1080/13873950701742754.

[42] W. Govaerts, Y.A. Kuznetsov, H.G. Meijer, MatCont (Version 7.1) [computer software], 2008, https://sourceforge.net/projects/matcont.

[43] R. Barrio, A. Shilnikov, Parameter-sweeping techniques for temporal dynamics of neuronal systems: case study of Hindmarsh-Rose model, J. Math. Neurosci. 1 (2011) 6:1–6:22, http://dx.doi.org/10.1186/2190-8567-1-6.

[44] G.N. Benes, A.M. Barry, T.J. Kaper, M.A. Kramer, J. Burke, An elementary model of torus canards, Chaos 21 (2) (2011) 023131, http://dx.doi.org/10.1063/1.3592798.

[45] N. Fenichel, Geometric singular perturbation theory for ordinary differential equations, J. Differential Equations 31 (1) (1979) 53–98, http://dx.doi.org/10.1016/0022-0396(79)90152-9.

[46] M. Wechselberger, Existence and bifurcation of canards in $\mathbb{R}^3$ in the case of a folded node, SIAM J. Appl. Dyn. Syst. 4 (1) (2005) 101–139, http://dx.doi.org/10.1137/030601995.

[47] P. De Maesschalck, F. Dumortier, R. Roussarie, Canard Cycles - from Birth To Transition, Springer, Cham, ISBN: 978-3-030-79233-6, 2021.

[48] T. Kolokolnikov, T. Erneux, J. Wei, Mesa-type patterns in the one-dimensional brusselator and their stability, Phys. D 214 (1) (2006) 63–77, http://dx.doi.org/10.1016/j.physd.2005.12.005.

[49] I. Gucwa, P. Szmolyan, Geometric singular perturbation analysis of an autocatalator model, Discrete Contin. Dyn. Syst. 2 (4) (2009) 783–806, http://dx.doi.org/10.3934/dcdss.2009.2.783.
[50] D.M. Abrams, S.H. Strogatz, Chimera states for coupled oscillators, Phys. Rev. Lett. 93 (2004) 174102, http://dx.doi.org/10.1103/PhysRevLett.93.174102.
[51] M.J. Panaggio, D.M. Abrams, Chimera states: Coexistence of coherence and incoherence in networks of coupled oscillators, Nonlinearity 28 (3) (2015) R67 – R87, http://dx.doi.org/10.1088/0951-7715/28/3/R67.
[52] Y. Maistrenko, S. Brezetsky, P. Jaros, R. Levchenko, T. Kapitaniak, Smallest chimera states, Phys. Rev. E 95 (2017) 010203, http://dx.doi.org/10.1103/PhysRevE.95.010203.
[53] T. Chouzouris, I. Omelchenko, A. Zakharova, J. Hlinka, P. Jiruska, E. Schöll, Chimera states in brain networks: Empirical neural vs. modular fractal connectivity, Chaos 28 (4) (2018) http://dx.doi.org/10.1063/1.5009812.
[54] C.R. Laing, Chimeras on a ring of oscillator populations, Chaos 33 (1) (2023) http://dx.doi.org/10.1063/5.0127306.
[55] F. Takens, Singularities of vector fields, Publ. Math. Paris 43 (1974) 47–100, http://dx.doi.org/10.1007/BF02684366.
[56] H. Broer, G. Vegter, Subordinate Šil'nikov bifurcations near some singularities of vector fields having low codimension, Ergodic Theory Dynam. Systems 4 (4) (1984) 509–525, http://dx.doi.org/10.1017/S0143385700002613.
[57] Y.A. Kuznetsov, O. De Feo, S. Rinaldi, Belyakov homoclinic bifurcations in a tritrophic food chain model, SIAM J. Appl. Math. 62 (2) (2001) 462–487, http://dx.doi.org/10.1137/S0036139900378542.